Behavior of Sn-Ag-Cu Solder Bumps During Thermal Cycling

Master Thesis
Materials Science and Engineering

Author:
Eleni Tsepi

6071090

Daily Supervisor:
Lara Barros Rebouças
NXP Semiconductors PDQC-Nijmegen

University Supervisor:
Prof. Dr. Maria J. Santofimia Navarro
Faculty of Mechanical, Maritime and Materials Engineering

TU Delft

NXP

Feb 2025- Oct 2025

ABSTRACT

The present study investigates the microstructural evolution of Sn-Ag-Cu (SAC) solder joints subjected to thermal cycling, with emphasis on recrystallization and grain orientation. Thermal cycling is the main failure source in reliability tests of electronic devices, yet its microstructural effects remain insufficiently understood. Although numerous studies have examined solder joint fatigue using numerical modeling, the early microstructural changes are often overlooked. To address this gap, the present work characterizes experimentally stages of thermal-cycling-induced microstructural evolution.

The evolution of SAC solder joints was characterized using Electron Backscatter Diffraction (EBSD) on two sets of samples. (i) joints thermally cycled for an increasing number of cycles and subsequently cross-sectioned, and (ii) pre-cross-sectioned joints analyzed after consecutive rounds of cycling. Two distinct recrystallization mechanisms, namely primary and continuous dynamic, were identified, stabilizing after three thermal cycling stages. Grain rotation toward the [001]Sn-substrate angle and activation of slip systems 4, 6, and 10 suggest a strong link to the initial reflow texture. Moreover, IMC coarsening which facilitates grain boundary unpinning and promotes crack initiation, was also observed. Recrystallized grains exhibited a decrease in Young's Modulus, likely associated with orientation effects.

Calculation of Geometrically Necessary Dislocation (GND) density and Stored Energy Density (SED), with the aim to link EBSD and numerical modeling, while adequate for a first estimation, showcases the need for improved integration methods. Finally, the use of pre-cross-sectioned samples for in situ study of microstructural evolution is not recommended due to stress relaxation effects.

LIST OF ABBREVIATIONS AND SYMBOLS

BGA : Ball Grid Array
CCD : Charge-Coupled Device
CTE : Coefficient of Thermal Expansion
DNP : Distance to the Neutral Point
EBSD : Electron Backscatter Diffraction
GNDs : Geometrically Necessary Dislocations
GOS : Grain Orientation Spread
GROD-Ang : Grain Reference Orientation Deviation Angle
HAGBs : High-Angle Grain Boundaries
HAZ : Heat Affected Zone
IMC : Intermetallic Compound
KAM : Kernel Average Misorientation
LAGBs : Low-Angle Grain Boundaries
PCB : Printed Circuit Board
RoHS : Restriction of Hazardous Substances
SAC : Sn-Ag-Cu alloy
SED : Stored Energy Density
SEM : Scanning Electron Microscopy
SF : Schmid Factor
SLID : Solid-Liquid Interdiffusion
SSDs : Statistically Stored Dislocations

CONTENTS

1. Introduction

In the semiconductor industry, soldering is considered the best joining technology for microelectronics assembly, as it provides mechanical and electrical connections between the integrated circuit and the Printed Circuit Board (PCB) [1]. SnPb alloys were used as solder materials until 2003, when the Restriction of Hazardous Substances (RoHS) came into force and prohibited the use of lead [2]. The need for lead-free solder materials arose, and extensive research on this topic is ongoing. Sn-Ag-Cu alloys emerged as strong candidates and have been broadly used by the industry. SAC presents outstanding properties for soldering applications, however, its more complex structure compared to SnPb contribute to a wider spread in reliability results [3, 4, 5], as shown Figure 1.

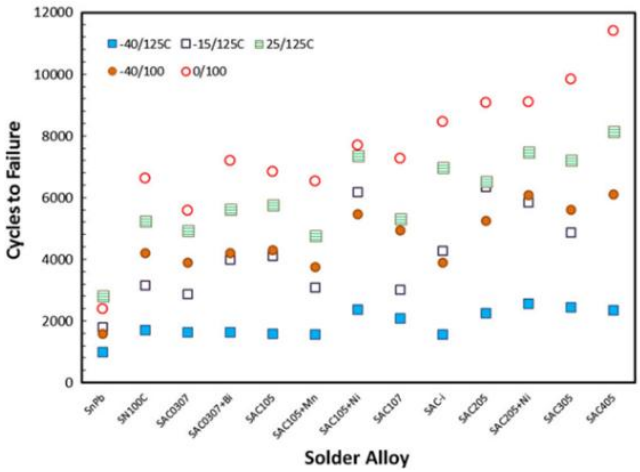

Figure 1: Comparison of characteristic lifetimes of multiple solder alloys for five different temperature profiles. Experiments were conducted on Ball Grid Array (BGA) components with 10 min dwell time. *[5]*

Solder joint cracking is known to be the most common cause of failure in electronic devices [6], with thermal cycling being the primary cause due to thermal expansion coefficient (CTE) mismatch [5]. There are two levels where CTE mismatch occurs. At the macroscopic level, CTE mismatch between the solder and the PCB results in cracking near the solder-package interface, driven by microstructural changes [7, 8]. At the microscopic level, mismatch between different phases or grains and mismatch attributed to the intrinsic β-Sn anisotropy, causes strain accumulation. Additionally, the geometric layout of the package influences strain distribution, with solders located farther from the center, a factor also known as Distance to the Neutral Point (DNP), experiencing higher stress levels and failing earlier [9, 10, 5, 11, 12].

Numerous publications are dedicated to the investigation of the effect of thermal cycling on the characteristic lifetime of SAC solders. Recent research has focused on numerical modeling in an effort to better understand the degradation mechanisms. However, microstructural features are often generated using randomized algorithms [12] or not taken into account in numerical models at all [13, 14]. Although researchers attribute failures to microstructural causes such as slip activity and recrystallization, these are rarely further investigated. Post-failure studies, provide valuable insights, but a thorough understanding of the deformation mechanisms still requires an in-depth study of the solder microstructure prior to failure.

In the present work, EBSD data during the early stages of deformation are collected in order to investigate how SAC solder microstructure evolves during thermal cycling and how this evolution correlates to the fatigue life of solder interconnects. This can potentially contribute to the development of high-accuracy predictive models.

2. Theoretical Background / State of the Art

2.1. Sn-Ag-Cu Solder Microstructure

Sn-Ag-Cu (SAC) near eutectic alloys have been widely used in the semiconductor industry [3, 4, 15]. Among these, the hypoeutectic SAC305 (96.5% Sn, 3% Ag, and 0.5% Cu wt.%) is the most commonly used solder often referred to as the "de facto standard Pb-free solder" [3, 4], providing the most interesting trade-off between high cost of Ag and melting temperature for most microelectronic applications. The phase diagram of SAC systems is demonstrated in Figure 2. The microstructure of a typical SAC solder consists of β-Sn dendrites, eutectic structure particles and non-uniformly distributed anisotropic IMC particles such as Cu_3Sn, scallop-type Cu_6Sn_5 and plate-like Ag_3Sn phases [16, 15, 17], as depicted in Figure 3. More information about the Sn-Ag and Sn-Cu interactions can be found in the corresponding binary phase diagrams in Figures A1-A2 in the Appendix.

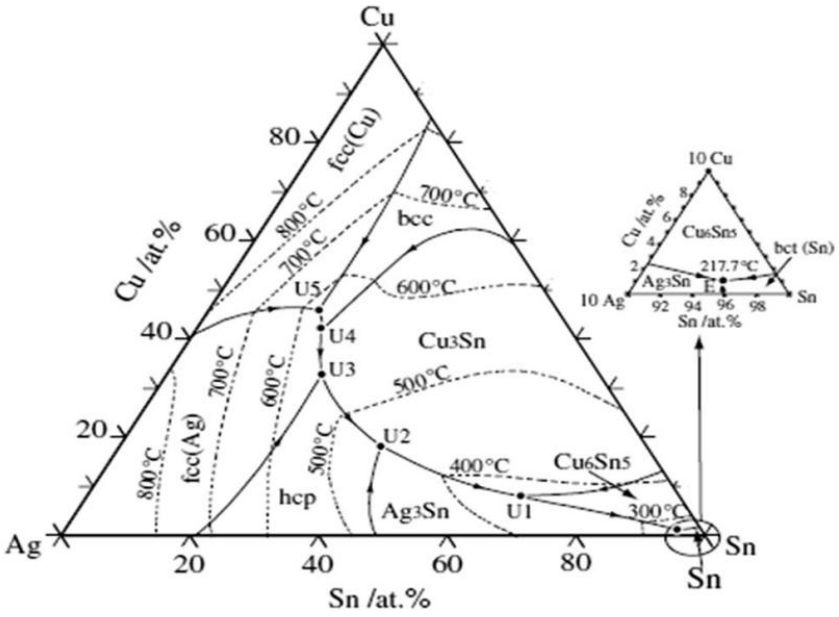

Figure 2: Sn-Ag-Cu ternary phase diagram *[16]*

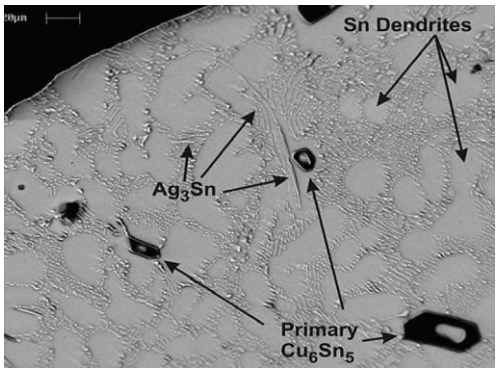

Figure 3: Typical microstructure of SnAgCu solder *[18]*

2.1.1 β – Sn system

SAC alloys have a β-Sn content of more than 90%. Subsequently, their morphology, mechanical, physical and chemical properties are directly related to the properties and structural characteristics of β-Sn, such as size, orientation, and morphology of β-Sn dendrites [2, 19]. The morphology of SAC solders can be distinguished in three structures, namely, single-grained, beach ball, and interlaced as shown in Figure 4. When a solder interconnect consists of more than two grains, they rotate by 60˚ around the [100] axis, forming a six-fold cyclic twinned morphology known as beach ball structure [20]. In such structures, three primary orientations dominate in the Sn grains and are related to growth from one single six-fold cyclic twinned nucleation point, which intersects with the <100> axis [21, 22]. The interlaced morphology is a complex dendritic structure where the grains are interpenetrating each other [21]. The morphology of the solder is linked to their size and solidification temperature. Interlaced morphology is more likely to be observed in smaller solders solidified below 170 °C, while beach ball structure is observed to a higher degree in larger solders solidified above 180 °C. At intermediate undercooling temperatures, interlaced and beach ball structures are both present, with the former being, preferentially, closer to the Sn nucleation point and transitioning to the latter further from the nucleation site [23, 24].

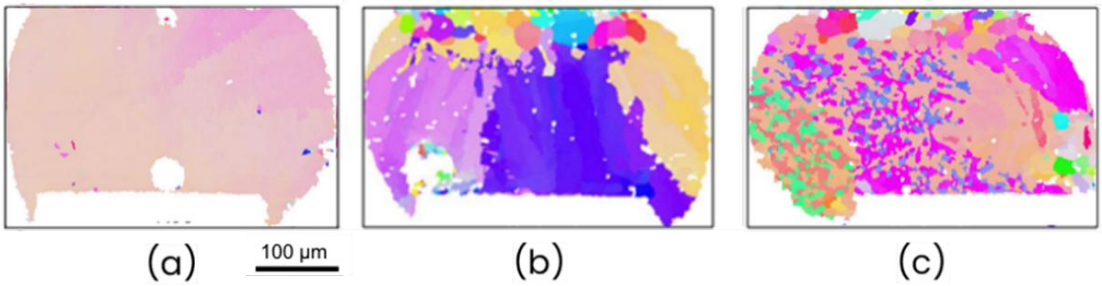

Figure 4: Grain morphologies of SAC solders. (a)single-grain (b) beach ball (c) interlaced. (Modified from reference *[25]*)

The crystal structure of β-Sn and the small amount of grains are responsible for the anisotropy and thus the microstructural non-uniformity and variability in mechanical properties and behavior of SAC solders under thermomechanical and electrical loadings [15, 20]. More specifically, β-Sn has a body-centered tetragonal crystal structure (c/a=0.5456), shown in Figure 5. This anisotropic nature is reflected in its CTE, which is highly direction dependent. The CTE along the [001] direction (c-axis) is $32.4 \cdot 10^{-6}$ K^{-1}, which is double the CTE in the [100] or [010] direction (a-axis), $16.5 \cdot 10^{-6}$ K^{-1} [7].
The impact of anisotropy on plastic deformation is demonstrated through the stiffness matrix of β-Sn, presented in the Appendix, where, C_{33} = 88.4 GPa, represents the stiffness along the [001] direction, which is significantly higher than the stiffness along the [100] and [010] directions, with $C_{11} = C_{22}$ = 72.3 GPa [26].

2.1.2 Intermetallic Compounds (IMCs)

Intermetallic compounds (IMCs) are often not included in numerical models, however they also contribute to the microstructural evolution during thermal cycling. There are two distinct types of intermetallics in the Sn-Ag system, the disordered hcp phase ζ, and the orthorhombic short-range ordered $Ag_3Sn(\varepsilon)$ [27, 28, 29]. Similarly, in the Sn-Cu system, the intermetallics formed are orthorhombic $Cu_3Sn(\varepsilon)$, hexagonal $Cu_6Sn_5(\eta)$ and monoclinic $Cu_6Sn_5(\eta')$ [27, 30]. In the temperature range of interest, near-eutectic SAC solders form $Ag_3Sn(\varepsilon)$, orthorhombic $Cu_3Sn(\varepsilon)$, and hexagonal $Cu_6Sn_5(\eta)$ [8], illustrated

in Figure 5. In Table A1 in the Appendix, the lattice parameters of all crystal structures present in SAC solders are listed.

Moreover, IMCs are also present in the form of layers between the interfaces of the solder with the copper pads of the PCB and the package. In particular, during solidification, solid-liquid interdiffusion (SLID) reactions occur, resulting in the formation of Cu_6Sn_5 [31, 32, 27]. After reflow, a thin layer of Cu_3Sn appears at the Cu_6Sn_5/Cu interface, that is too thin to be observed yet it may grow with isothermal aging [27, 29].

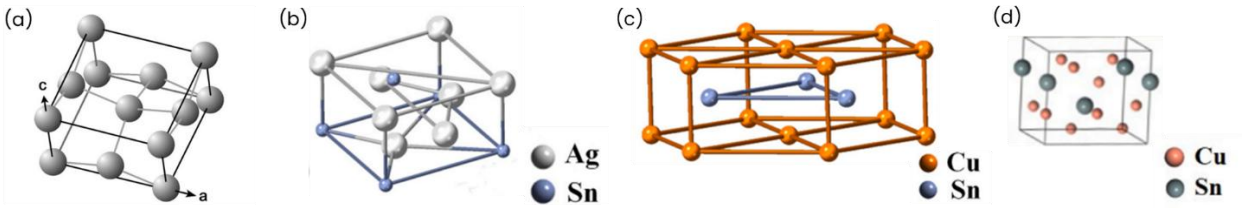

Figure 5: Crystal structure of β-Sn and IMCs observed in SAC. (a) body-centered tetragonal β-Sn *[33]* (b) orthorhombic $Ag_3Sn(\varepsilon)$ (c) hexagonal $Cu_6Sn_5(\eta)$ (d) orthorhombic $Cu_3Sn(\varepsilon)$ *[34, 35]*

The Sn-Cu binary phase diagram indicates that below 189 °C hexagonal $Cu_6Sn_5(\eta)$ transforms into monoclinic $Cu_6Sn_5(\eta')$. The attachment of solder of electronic packages occurs at temperatures above 200 °C, where $Cu_6Sn_5(\eta)$ is stable while electronic components operate at temperatures below 189 °C, where the $Cu_6Sn_5(\eta')$phase is stable. At room temperature, the transformation does not take place within a practical timeframe due to kinetic constraints. On the contrary, at elevated temperatures such as those reached due to local heating during the operation of the components, the time required reduces significantly [27, 36]. The n-to-n' transformation is accompanied by a 2.15% change in volume and thus, has the potential to generate stresses and induce cracking of the solder affecting its reliability [37].

2.2. Microstructure Driven Deformation in SAC Alloys

To better understand the role of microstructure in the reliability of solders, it is essential to delve into the microstructural features that contribute to the degradation. In particular, it has been consistently reported in post-failure studies in the literature that grain orientation, slip activity and recrystallization, IMC grain coarsening and strain accumulation are factors affecting the thermomechanical response of solders.

2.2.1. Grain Orientation

Experimental results [38] show that there is dependence of the thermomechanical response on Sn grain orientation. This originates from the highly anisotropic nature of β-Sn, which is reflected in the significant difference between the CTE and Young's Modulus along the [001] and [100]/[010] directions, as shown in Figure 6. Notably, β-Sn is stiffer along the [001] direction, which also has the highest CTE. The combination of high CTE and stiffness, along the same direction, can lead to increased internal stresses. Moreover, their dependence on direction may cause directional expansion during thermal cycling, the severity of which, is highly affected by the orientation of the β-Sn crystal. It is supported in the literature, that when the c-axis of β-Sn is parallel to the substrate, the solder has higher chance of failing during thermal cycling [20, 39, 40].

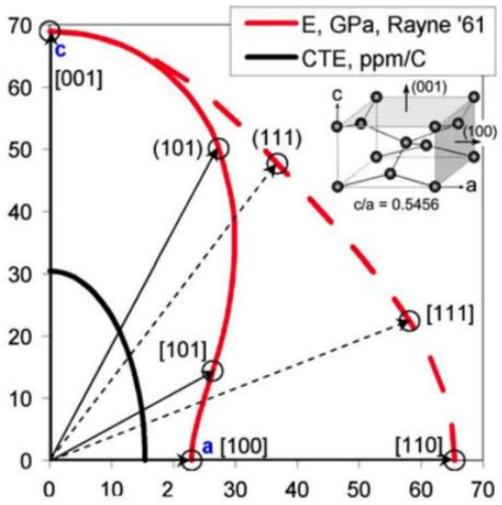

Figure 6: Variation of elastic and thermal expansion properties due to Sn crystal anisotropy *[38]*

The influence of grain orientation is more pronounced when considering different grain morphologies. In the case of a single-grained morphology, the solder has only one dominant orientation and thus is expected to have, overall, a more heterogeneous behavior. When the grain morphology is beach ball like, three orientations are dominant. These orientations are the result of six-fold cyclic twinned nucleation around a common axis [21, 22]. This means that a group of grains, may respond mechanically as a single crystal when uniaxially loaded along the common axis, or as a multicrystal in other directions [38]. In interlaced morphologies, although the structure is more complex, three cyclic twinned grain orientations are also dominant [23, 41]. However, their response will differ from the symmetric beach ball structure and lead more to homogeneous behavior.

2.2.2. Dislocations and Slip Activity

Dislocations are line defects that act as carriers of plastic deformation, and can be classified into two types, geometrically necessary dislocations (GNDs) and statistically stored dislocations (SSDs) [42, 43]. In particular, GNDs are necessary to maintain geometrical compatibility between grains by accommodating lattice curvature during non-uniform plastic deformation [44, 45, 46], as shown in Figure 7. On the contrary, SSDs randomly form opposite-sign pairs (dipoles) during uniform plastic deformation and do not contribute to lattice curvature [44, 45, 46].

GNDs can be distinguished in edge, screw and mixed dislocations [44, 42, 47, 43]. Illustrations of the corresponding lattice distortions are shown in Figure 8. An edge dislocation is represented as an additional plane in the lattice, whose edge, is the dislocation line. A screw dislocation denotes the circular motion around a given point, also known as dislocation core, which results in the helical displacement of atoms resembling the motion of a screw. The dislocation line of a screw dislocation aligns with the dislocation core. A mixed dislocation is the combination of an edge and screw dislocation and the dislocation line is a curve instead of a straight line [43, 47]. Dislocation lines typically terminate either at a free surface or an interface like grain or phase boundaries [29, 47].

Dislocations are characterized by the Burgers vector, b, which quantifies the magnitude and direction of the distortion introduced by the dislocation [43]. In an edge dislocation the Burgers vector is perpendicular to the dislocation line, therefore, the dislocation moves parallel to the shear stress applied

while in screw dislocations, the Burgers vector is parallel to the dislocation line resulting in dislocation motion towards the perpendicular direction [47]. The motion of dislocations contributes to strain accumulation leading to changes in the microstructure of the material.

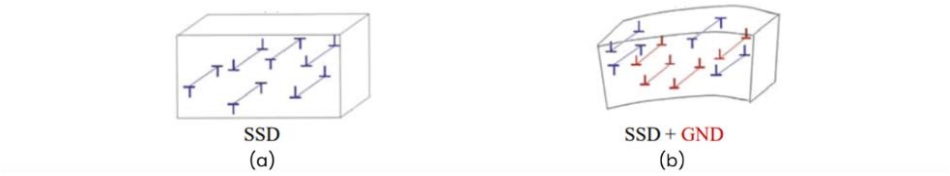

Figure 7: Effect of (a) SSD and (b) GND accumulation on crystal lattice curvature *[46]*

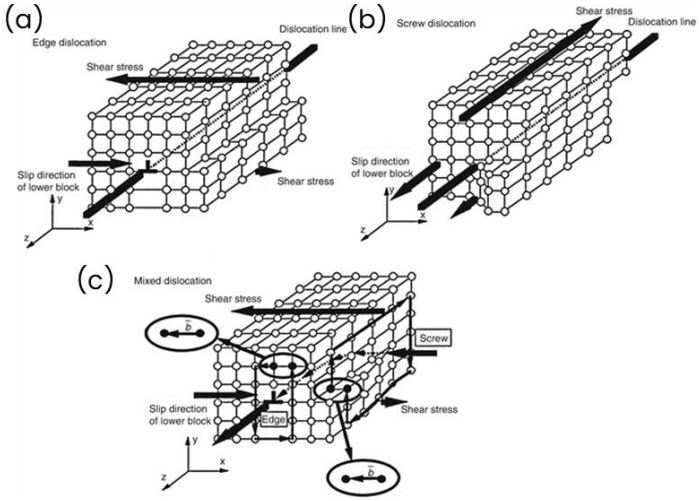

Figure 8: Dislocation types (a) Edge dislocation (b) Screw dislocation (c) Mixed dislocation *[48]*

Dislocations cannot move across grain boundaries, especially of high misorientation angle, leading to the formation of dislocation pile-ups. If the number of dislocations exceeds a critical threshold, these induce a cumulative stress that is able to stimulate a slip system in the adjacent grain. A slip system, is a preferential plane and direction along which slip occurs [29, 47, 43]. In β-Sn-rich systems slip is the dominant deformation mechanism between 18 °C and 150 °C [49, 50, 51], making the role of slip activity in the reliability of SAC solders, particularly significant.

When the grain orientation with respect to loading direction is favorable, a slip system is activated. A crystal orientation may correspond to multiple slip systems. Which one will activate can be determined by the Schmid factor, *m*, which relates the applied stress, σ, with the resolved shear stress, τ_{RSS}, on each slip system through the equation [43]:

$$\tau_{RSS} = m \cdot \sigma \quad \text{(E1)}$$

$$m = \cos\varphi \cos\lambda \quad \text{(E2)}$$

Where, φ, is the angle between the slip plane normal and the load direction and λ, is the angle between the slip direction and the load direction. The slip system with the highest Schmid factor, has the highest resolved stress for a given applied stress and thus, will activate first and initiate microstructural evolution [39, 8]. In β-Sn crystals, there are 32 known slip systems that can be activated [52]. These are listed in

detail in Table A2 in the Appendix. Operating slip systems create slip bands, and can be identified either by slip trace analysis [8] or Schmid factor mapping [53].

The activation of a slip system involves the movement of dislocation, edge or screw, depending on the orientation of the dislocation line with respect to the Burgers vector. In edge dislocations the Burgers vector is perpendicular to the dislocation line, there are 32 independent edge GNDs. In screw dislocations, the Burgers vector is parallel to the dislocation line, and thus, slip systems with the same slip direction share the same values of screw GND densities. Subsequently, the number of independent screw GNDs in β-Sn crystals, amounts to 15 [42, 54].

2.2.3. Subgrain Formation and Recrystallization

Slip system activation leads to gradual lattice rotation along a single rotational axis. This increases the stored energy in the region, resulting in the formation of subgrain boundaries and orientation gradients within the grains [8, 52]. This subgrain formation is part of a recovery mechanism, where dislocations rearrange and partially annihilate, releasing the stored energy of the system in the high-strain regions [55, 56]. The subgrain regions are characterized by the increase of low-angle grain boundaries (LAGBs) and are correlated with high dislocation density.

With further subgrain rotation, dislocations are absorbed into LAGBs, increasing the misorientation and thus, leading to the formation of high-angle grain boundaries (HAGBs) [57]. More precisely, the network of HAGBs in the high-strain regions separates highly misoriented grains that form a recrystallized region [55]. The interface energy of grains separated by HAGBs is larger than the required energy for separation due to the high misorientation, therefore HAGBs are prone to crack initiation and propagation [39, 56, 40].

Recrystallized grains, often found in thermally cycled SAC solders, show almost no orientation gradient nor internal strains compared to the parent grains (subgrain region) [8, 58] and have low dislocation density [59, 56, 60, 25].Moreover, recrystallized grains tend to experience a decrease in hardness [20, 56, 59, 60, 61, 51, 57, 62], which can reach up to 39%, compared to the as-reflowed microstructure in SAC [56, 60]. This is attributed to stress release and precipitate coarsening [59, 51] as well as orientation changes [20]. Given the susceptibility to intergranular cracking in the recrystallized region [23, 22, 5, 55, 51, 59, 60], the lifetime and reliability of the material is affected by crack propagation once recrystallization occurs [39, 56, 40].

2.3. Electron Backscatter Diffraction (EBSD) for Microstructural Characterization

Researchers attribute failures to intrinsic β-Sn anisotropy induced microstructural causes such as slip activity, recrystallization, grain boundary sliding and decohesion [7]. The majority of the early studies focusing on microstructure evolution use SEM and/or cross-polarized light [23, 63, 10, 64, 5, 22] to visually inspect grain morphology and orientation, slip bands and crack propagation. Besides the fact that these methods cannot provide quantified data, concerns have been raised on whether the observations based on cross-polarized light are accurate due to its low resolution [51].

The limitations of cross-polarized light are highlighted by contradicting research on transgranular cracking. While most researchers agree that intergranular cracking dominates in recrystallized regions [23, 22, 5, 55, 51, 59, 60], some suggest transgranular cracking can occur under mild or aggressive thermal

cycling [8, 65]. This contradiction may arise because cross-polarized light imaging often fails to reveal newly developed grains or subgrain boundaries, potentially leading to misidentification of crack paths [51]. Subsequently, the need for more advanced microstructure characterization methods with higher resolution and the ability to quantify microstructural features arises. In this way, microstructural evolution can be studied more thoroughly with a lower risk of result misinterpretation. Electron Backscatter Diffraction (EBSD) is a technique capable of meeting these requirements and has already been implemented in reliability studies. Nevertheless, the majority of these studies are limited to the post-failure state, single-grain solders, while features like grain size and misorientation are rarely quantified over time. Additionally, there is hardly any correlation between EBSD data and the electrical or mechanical behavior of solders. Linking microstructure changes with macroscopic material properties could be beneficial for better understanding of material behavior as well as the development of more accurate prediction models and digital twins.

Scanning Electron Microscopy (SEM) is a material characterization technique where a scanning electron beam is used, instead of light, to generate high-resolution images up to the nanometer scale [66]. Electrons are emitted from an electron gun forming a beam, that is focused on the sample surface using electromagnetic lenses. As the beam passes through the column under vacuum, coils assist in preventing electron deflection while the lenses adjust the beam diameter to a few nanometers probe. The incident electrons penetrate a few micrometers in the material surface and generate backscatter electrons, secondary electrons and x-rays that are collected from different detectors. Backscattered electrons (BSEs) are elastically scattered and provide information about the composition and the topography of the sample surface. Secondary electrons (SEs) are inelastically scattered and provide information about the topography of the surface while x-rays give information about the composition [66, 67].

Electron Backscatter Diffraction (EBSD) also known as backscatter Kikuchi diffraction (BKD) or backscatter electron Kikuchi diffraction (BEKD), when employed as an additional characterization technique to a SEM, enables detailed microstructure characterization [68, 45]. This includes grain orientation, grain size and distribution, grain boundary distribution, misorientation angles and relations, phase identification, texture and dislocation density mapping.

The working principle of EBSD is based on the interaction of the incident beam and a small volume of the crystalline material, usually referred to as the interaction volume. This volume extends up to 20 nm below the sample surface and spreads laterally along the projected area of the incident beam [68]. Backscattered electrons, generated by the interaction of the SEM beam with the sample surface, are captured using a fluorescent screen coupled with a lens that projects the image onto a charge-coupled device (CCD) camera [69]. In Figure 9, a representation of the set-up as well as the working principle of EBSD is shown. When the electron beam hits the sample, portion of the electrons is diffracted by crystallographic planes at an angle θ, in accordance with Bragg's law [45, 70]:

$$n\lambda = 2dsin\theta \tag{E3}$$

where, *n* is the order of reflection, λ, the wavelength and, *d*, the interplanar spacing of a family of planes (hkl) [68].

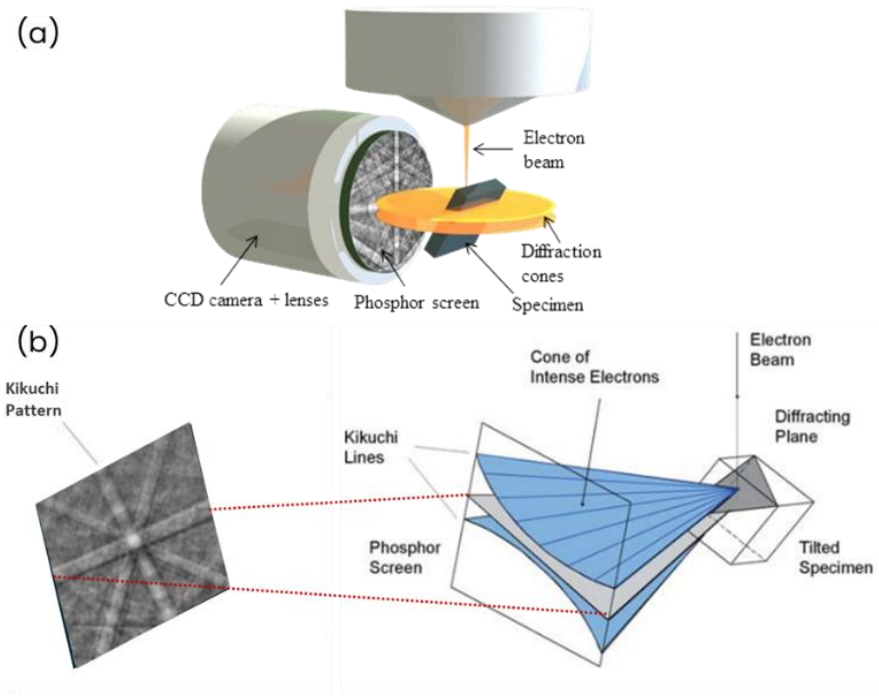

Figure 9: (a) Illustration of a conventional EBSD set-up. *[71]* (b) Working principle of EBSD. Schematic of diffracting cones with respect to reflecting plane, the specimen and the phosphor screen. (Modified from references *[72, 73]*)

For each family of planes, diffraction occurs in all directions generating two Kossel cones, shown in Figure 10, that expand under a 90˚- θ angle with respect to the diffracting plane normal. The intersection of the Kossel cones with the phosphor screen forms the edges of the Kikuchi bands with an angular distance of 2θ. Subsequently, the width of the Kikuchi bands is directly related to the interplanar spacing of the diffracting crystallographic planes [68, 45]. The intersections of Kikuchi bands form zone axes, which correspond to crystallographic directions shared by all the intersecting planes. A Kikuchi pattern, is the collection of Kikuchi bands and their intersections, containing information about interplanar spacing as well as interzone (angles between zone axes) and interplanar angles (angles between planes) that reflect the crystal structure, orientation and symmetry [45, 8]. The process of identifying the poles in a pattern is called indexing.

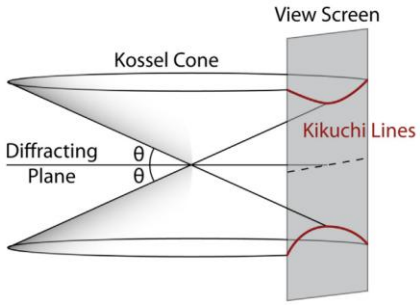

Figure 10: Kossel cones generated by diffracted electrons, in accordance with Bragg's law. *[70]*

The indexing process, demonstrated in Figure 11, is divided into three discrete steps. These are band detection, zone axes identification and determination of crystal orientation from interplanar and interzone

angles [8]. Band detection is achieved through the Hough transformation where each Kikuchi band is represented as a point in the Hough space. Then, interzone angles are measured and compared with values from known crystal structures in order to be identified. Based on the indexed zone axes, the crystal orientation can be defined from which the rotation (or orientation) matrix will be calculated.

The rotation matrix links the crystal coordinate system with the sample coordinate system through the Euler angles, φ_1, Φ and φ_2, which are the primary output of EBSD [8, 45]. It describes a three-step rotation process that transforms the sample coordinate system to the crystal coordinate system. The first step is a rotation of φ_2 degrees around z-axis, followed by a rotation of Φ degrees around x-axis and finally, a rotation of φ_1 degrees around z-axis, as demonstrated in Figure 12. The order in which the rotations are applied is crucial because each rotation changes the coordinate system of the next one. Therefore, different order leads to different final orientation [8, 74].

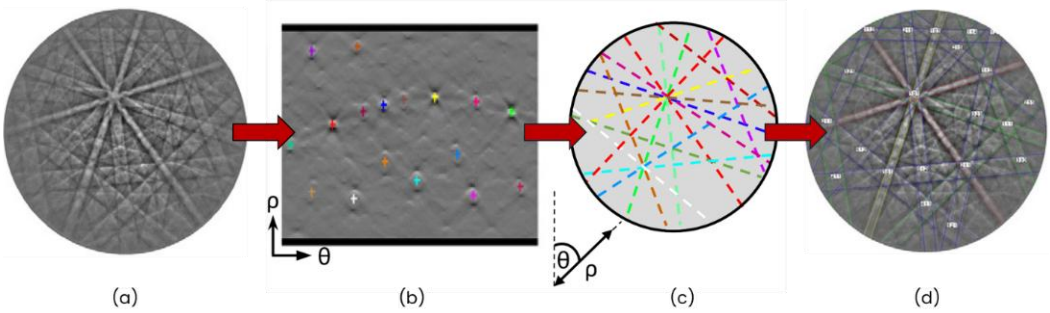

Figure 11: Schematic of Hough-based indexing. (a) Experimental pattern. (b) Hough transformation. (c) Band detection. (d) Indexed pattern (Modified from reference *[74]*)

$$\mathrm{R} = \mathrm{R}_{\varphi_1}\mathrm{R}_{\Phi}\mathrm{R}_{\varphi_2} = \begin{bmatrix} \cos\varphi_1 & -\sin\varphi_1 & 0 \\ \sin\varphi_1 & \cos\varphi_1 & 0 \\ 0 & 0 & 1 \end{bmatrix}\begin{bmatrix} 1 & 0 & 0 \\ \sin\varphi_1 & \cos\Phi & -\sin\Phi \\ 0 & \sin\Phi & \cos\Phi \end{bmatrix}\begin{bmatrix} \cos\varphi_2 & -\sin\varphi_2 & 0 \\ \sin\varphi_2 & \cos\varphi_2 & 0 \\ 0 & 0 & 1 \end{bmatrix} \quad \text{(E4)}$$

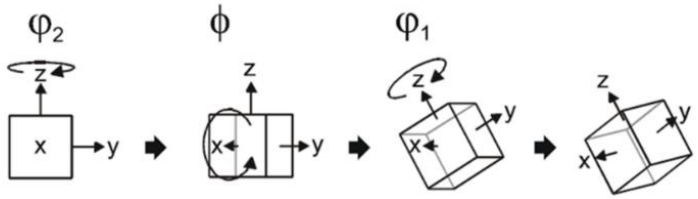

Figure 12: Rotation of the crystal around its own axes, in accordance with the Euler angles. Initially, the coordinate system is coincident with the fixed sample coordinate system. *[75]*

Moreover, the quality and accuracy of EBSD indexing are strongly influenced by the quality of the collected data and thus, the parameters tuned prior to data acquisition. The main adjustable parameters in EBSD are the acceleration voltage, beam current, tilt angle, step size and working distance [69]. The acceleration voltage influences the energy of the electrons and the interaction volume in terms of depth of penetration. Beam current is related to signal strength while a combination of high acceleration voltage and low beam current minimizes the signal to noise ratio enhancing spatial resolution [69]. The specimen is typically placed in the SEM chamber at an inclination of 70˚ with respect to the beam, using a 45˚ pre-tilted stage. A relatively large angle between the beam and the sample surface accommodates

an increase in the interaction volume and subsequently, the amount of backscattered electrons that can be diffracted [45], enhancing the resolution of Kikuchi bands [69].

The scanning step size determines the resolution of the pattern and depends on the size of the area of interest and the analytical needs [8, 69, 76]. For grain size measurements, phases and grain boundaries, a relatively coarse step size (i.e., 3-10 μm [8]) can be used. Larger step sizes can be used for texture measurements with little regard for the grain size. If the sample is unknown, then with a quick scan, the average grain size can be estimated and based on that, the step size can be determined. Typically, a step size equal to one tenth of the average grain size is used [76].

For more detailed study of localized orientation gradients, grain boundary distributions, local texture, fatigue cracks, and accumulated strain it is more sensible to use a smaller step size (i.e., 0.25-1 μm [8]). For strain mapping specifically, smaller step sizes between 0.05 and 0.5 μm can be used [77, 78, 79]. It should be taken into consideration that the smaller the step size is, the longer the acquisition time will be. For this reason, the step size needs to be determined also based on the tool availability [80].

2.4. EBSD Mapping and Microstructural Interpretation in SAC Alloys

Electron Backscatter Diffraction (EBSD) enables detailed microstructure characterization [68, 45] through the mapping of features such as grain orientation, grain size and distribution, grain boundary distribution, misorientation angles and relations, phase identification, texture and dislocation density. In Figure 13, different types of EBSD results are classified according to their interpretation in relation to microstructure evolution.

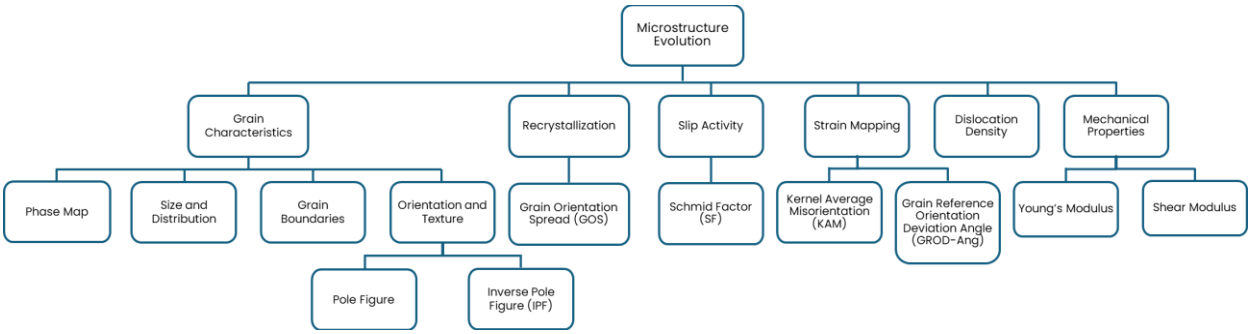

Figure 13: Classification of EBSD data based on their interpretation in relation to microstructure evolution

Phase identification and mapping, Figure 14(a) is possible with EBSD, as long as the existing phases are known to the operator. Grain characteristics such as grain size and distribution can be exported in the form of grain lists while grain boundaries are classified based on their type, LAGBs (0-10° and 10-15°) and HAGBs (>15°) shown in Figure 14(b). The orientation of the grains is visualized through the pole and inverse pole figures (IPF), Figure 14(d-f). To monitor the c-axis orientation with respect to the substrate, the [001] pole figure projected on the XZ plane can be used assuming an acquisition surface in the XY plane. Additionally, IPF-colored maps reveal the orientation of the grains with respect to a reference axis, typically along the loading direction [81]. These maps provide an overview of the different orientations between neighbouring grains in the sample, as shown in Figure 14(c). Grain Orientation Spread (GOS) maps, Figure 14(g), visualize the average deviation between measurement points and the mean orientation of the grain. Recrystallized grains typically show low GOS values due to their low content in

dislocations [82], therefore, GOS maps can be used for the identification of recrystallized grains, as illustrated in Figure 14(h). Moreover, visualization of the Schmid Factor (SF) for every slip system of a given metal facilitates the identification of active slip systems. Grains where a particular slip system is active typically appear in darker shades of color compared to grains where the same system is inactive, as shown in Figure 14(i). A more detailed analysis of slip activity can be achieved by exporting the SF values for each grain.

Complementary to slip activity analysis, strain mapping through the Grain Reference Orientation Deviation Angle (GROD-Ang) and Kernel Average Misorientation (KAM) maps provide insights into local plastic deformation and strain accumulation within the sample, as shown in Figure 14(j-k). The localized sensitivity derives from the way these parameters are calculated. GROD-Ang values are calculated per pixel and correspond to the deviation of each pixel's orientation from the average orientation of the grain. KAM values are calculated per pixel and represent the misorientation between the pixel and its nearest neighbors [46, 83]. Because these values are calculated per pixel, they can capture localized changes. However, they vary with step size and therefore, they are not recommended for identifying recrystallized grains [83]. GNDs are associated with lattice curvature and thus, misorientation. Therefore, GND density can be expressed as a linear function of KAM and mapped accordingly [46, 83, 44, 84], as shown in Figure 14(l). Mechanical properties such as Young's Modulus and Shear Modulus can be obtained from EBSD data, Figure 14(m-n). While more accurate values require experimental validation, EBSD-based estimations can provide a useful approximation of how anisotropic elastic behavior varies with grain orientation.

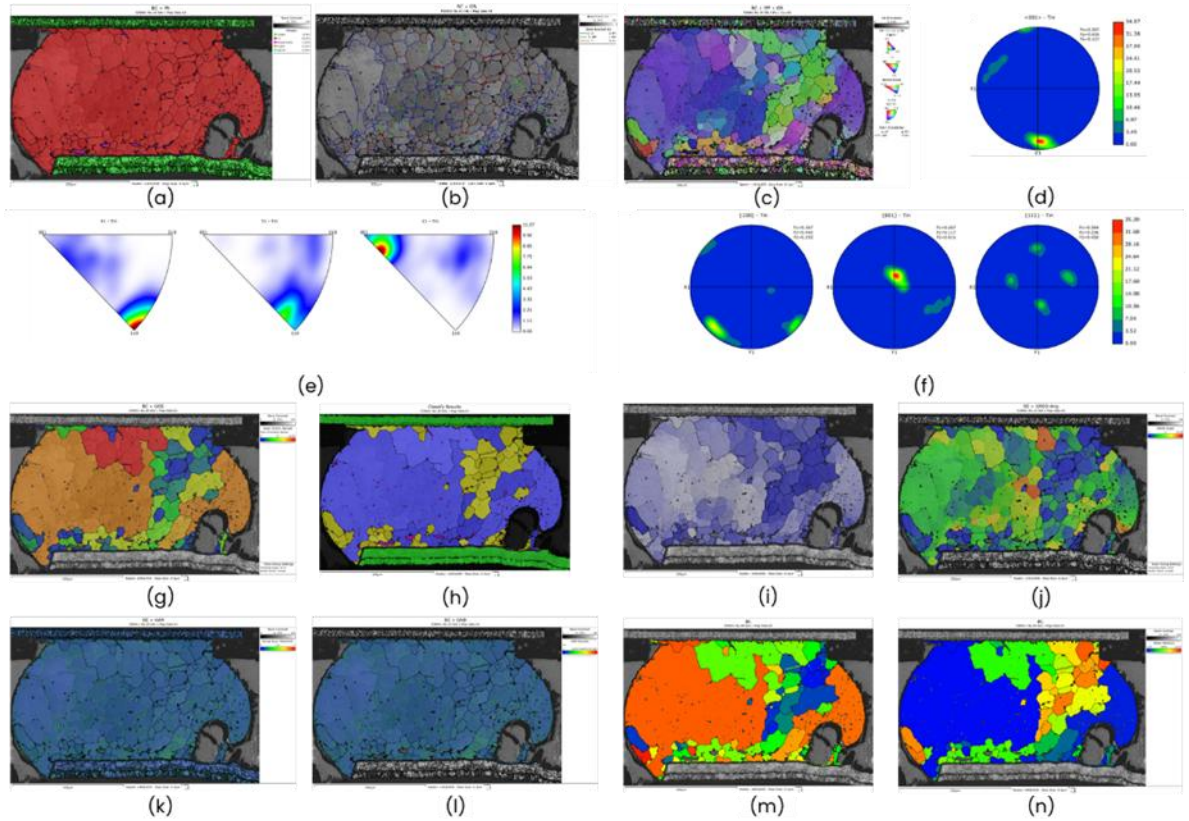

Figure 14: (a)Phase map (b) Sn grain boundaries distribution (c) IPF-colored orientation map expressed in Y axis orientation (d) [001]Sn pole figure (e) Sn IPF figures (f) Sn pole figures (g) GOS map (h) Classification between recrystallized and deformed grains (i) Schmid factor map (j) GROD-Ang map (k) KAM map (l) GND map (m) Young's Modulus map (n) Shear Modulus map.

Together, these EBSD outputs provide a better understanding of the microstructural state and evolution in SAC alloys. Additionally, they provide the foundation for the calculation of the Stored Energy Density (SED), a quantity widely recognized as a microstructure-sensitive and highly localized damage indicator, that can be used to determine the crack initiation point and the extent of fatigue damage [25, 42, 85]. SED can be calculated from:

$$\mathrm{SED} = \frac{1}{2} G\, \rho_{GND}\, b^2 \tag{E5}$$

where, G, is the shear modulus (GPa), ρ_{GND}, the GND density ($10^{14}/m^2$) and b, the magnitude of the Burgers vector [46, 83, 86, 42].

3. Experimental Procedure & Analysis

3.1. Sample Description

The samples used are SAC solders forming an interconnection between a BGA components and a PCB, as shown in Figure 15(b). The configuration as well as an optical microscopy image of a sample is shown in Figure 15(a, c) while, in Figure 15(d, e), optical images of a corner joint are demonstrated.

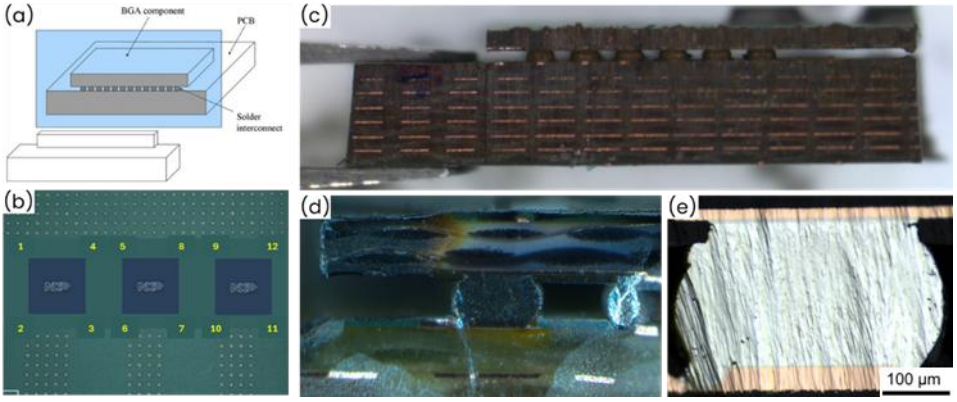

Figure 15: (a) Sample configuration *[57]* (a) Optical microscopy image of a BGA package after laser ablation (b) – (c) Optical microscopy images of a BGA corner bump after cross-section ion-milling (scale)

3.2 Thermal cycling

In total, two sets of samples were investigated. The first set consists of ten samples that were thermally cycled for a different number of cycles, in pairs of two, to a specific stage of the degradation process, ranging from Stage 0 to Stage 5. Stage 0 indicates that the condition of the solder is as-reflowed and no additional stress has been induced, while, Stage 5 indicates that the solder has been cycled until failure. The second set includes two samples that were pre-cross-sectioned and thermally cycled in an interruptive manner. Then, the sample undergoes thermal cycling between -40 and 125 ˚C with 15 minute dwell and ramp times [12]. The thermal cycling profile is illustrated in Figure 16. More details about the samples and the stages of thermal cycling they are subjected can be found in Table A4 in the Appendix.

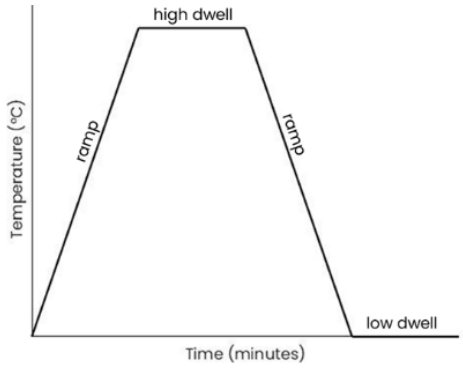

Figure 16: Thermal cycling temperature profile.

3.3. Cross-Section Protocol

While optimization of acquisition parameters is crucial for the quality and accuracy of EBSD indexing, the condition of the acquisition surface has great impact as well. Subsequently, EBSD requires a thorough sample preparation process to produce a flat and damage-free surface that is capable of generating high-quality Kikuchi patterns. For this purpose, typically techniques like laser ablation cross sectioning and ion-milling are employed. After thermal cycling, the applied cross-sectioning protocol consists of cross-sectioning using laser ablation followed by a charge sinking-coating step, and finally, targeted ion-milling on the corner solder joint of the BGA component. In this way, the introduction of mechanical stresses during sample preparation is avoided, enhancing the integrity of the sample. As a result, any microstructural changes observed will be attributed to thermal stresses induced by thermal cycling. Stage 0 cross-sections were prepared in the same manner.

Laser Ablation

Laser cross-sectioning is gaining more ground over the years as an alternative to blade (saw) cross-sectioning in the semiconductor industry due to the higher cutting speed, lower damage risk and less residual stresses [87]. The working principle has its foundation in the interaction between the laser and the material, which depends on the laser beam characteristics, the laser pulse properties and the optical properties of the material. The energy of the incident laser beam is partially absorbed leading to a buildup of free electrons while forming an electron plasma that interacts with the laser. When the electron plasma density reaches a critical value, ablation occurs, causing phase changes in the bulk material [87]. The intense heat under which the phase changes occur, lead to the creation of the heat affected zone (HAZ), as shown in Figure 17, where the microstructure and the properties of the material are altered.

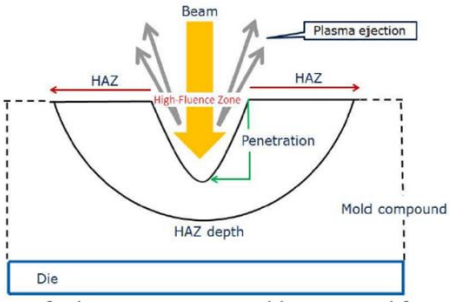

Figure 17: Illustration of HAZ formation during laser ablation *[88]*

Laser ablation is applied as the initial step in sample preparation for cross-sectioning, using a CLC Falit laser system. The recipe applied, shown in Table 1, has been developed and optimized to result to the minimum HAZ, and is suitable for the particular product under study. It includes fast passes and low energy so that only the targeted area is ablated.

Table 1: CLC Falit laser system settings for laser ablation

Parameter	Value
UV Current	35
Qswitch	40
Speed	400
Qrelease	2

Ion - milling

Ion – milling is a technique widely used for material removal, typically as the final stage of sample preparation. The working principle of ion – milling is based on physical etching through the sputtering effect, where atoms are removed from the sample surface by inert gas ions accelerated by an electric field. This process eliminates surface contamination and artifacts, resulting in high-quality cross - sections. Argon gas is commonly used as the ion source, among other gases like gallium and xenon, because it has lower risk of infiltrating the material and causing compositional changes that could affect quantitative elemental analysis [89, 90, 91, 92]. A schematic diagram of the cross-section milling set-up is shown in Figure 18(a). The part of the sample extending beyond the mask edge is the area to be ion-milled. The argon ion beam sputters the excess material along the mask edge, as shown in Figure 18(b). Since sputtering is the result of dislodging surface atoms, some degree of surface damage is expected [93]. This can be in the form of the curtaining effect where lines and irregular surfaces are caused by uneven milling across heterogeneous materials, for instance between the Sn matrix and IMCs such as Ag_3Sn, Cu_3Sn and Cu_6Sn_5. Surface damage can also be present in the form of rippling which is attributed to the large ion size compared to those in the sample [92]. However, these effects can be minimized by completing the process with a low-energy acceleration voltage [93]. Additionally, to ensure evenly milled surface, the sample holder rotates over a range of ±15 – 40˚ [90, 89].

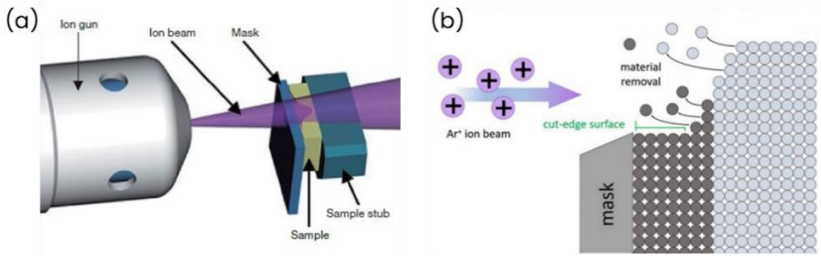

Figure 18: (a) Schematic diagram of cross - section milling set up. *[90]* (b) Illustration of the ion – milling process. (Modified from reference *[92]*)

Ion milling is applied to remove the HAZ and create a surface suitable for EBSD, using a Hitachi Ion-Milling System ArBlade 5000. The recipe applied, provided in Table 2, has been developed and optimized to result in a high-quality cross-section minimizing the risk of ion implantation, ion induced damage, curtaining and rippling. Prior to ion milling, a 5nm layer of Pt coating is deposited on the sample, to provide

conductivity and reduce drift effects in the SEM. The coating covering the targeted area is removed during ion milling, while the surroundings of the sample remain grounded, sinking any undesirable charges.

Table 2: Hitachi Ion-Milling System ArBlade 5000 settings for ion-milling

Parameter	Value
Gas used	Argon
Acceleration voltage	8 kV
Discharge voltage	1.5 kV
Gas flow	0.11 cm^3/min
Stage mode	40˚
Maximum milling width	1 solder bump
Duration	4 hours

3.4 Characterization Techniques

3.4.1. Scanning Electron Microscopy (SEM)

A Verios 460L by FEI SEM is applied for visual inspection of the sample surface and solder interfaces, as well as microstructural characterization and IMC thickness measurements. The settings are optimized to minimize charging effects and improve measurement accuracy and are shown in Table 3. All images were obtained at the working distance of EBSD, which is 10mm, to ensure the integrity of the lens.

Table 3: Verios 460L settings for IMC thickness measurements

Parameter	Value
Acceleration voltage	7 – 20 kV
Beam current	0.2 – 3.2 nA
Working distance	10 mm
Tilt angle	45˚ - 70˚

3.4.2. Electron Backscatter Diffraction (EBSD)

A Symmetry S3 EBSD detector by Oxford Instruments is used for detailed microstructure characterization of SAC solder bumps. The applied settings are listed in Table 4. Data analysis was conducted using the Aztec Crystal software by Oxford. The extracted maps are listed in Table 5 along with the appropriate settings.

Table 4: Symmetry S3 settings for EBSD analysis

Parameter	Value
Acceleration voltage	20 kV
Beam current	3.2 nA
Tilt angle	70˚
Working distance	10 mm
Step size	0.3 µm
Exposure time	4 ms
Magnification	approx. 500

Table 5: EBSD Map settings

Order	Map	Settings	Comments
1	Phases	Default	
2	IPF and Grain Boundaries	Set Y0 as reference axis	Loading direction//Y0,Y1
3	Grain Boundaries	Exclude all phases but Tin Set 2 - 10˚ LAGBs 10 - 15˚ LAGBs >15˚ HAGBs	Extract boundary list per phase
4	Phase Boundaries	Include only boundaries between Sn-IMCs	Extract boundary list
5	GROD-Ang	Exclude all phases but Tin	
6	KAM	Exclude all phases but Tin Kernel size 3x3	Smallest Kernel size for increased precision.
7	GND	Exclude all phases but Tin Kernel size 3x3 b = 1 [001] alpha = 3	Settings need to align with KAM map settings. Burgers vector for Sn crystals. Alpha depends on boundary type. alpha=3 for mixed type
8	Schmid Factor	Exclude all phases but Tin Loading direction Y0,Y1	Separate map for every slip system. Extract the SF list per slip system.
9	IPF	Default for Tin	
10	Pole Figures	Default for Tin and <001> Tin projected on the XZ plane	For every pole in the <001>XZ figure, measure the angle between pole and Y0-axis
11	Disorientation Axes	Exclude all phases but Tin High Angle in Crystal Coordinates Low Angle in Crystal Coordinates	
12	Young's Modulus	Loading direction Y0,Y1	Use appropriate compliance matrix Extract value list
13	Shear Modulus	Loading direction X0,X1 Shear plane XZ	Extract value list
14	GOS		Extract grain lists per phase (include ID, area, equivalent circle diameter, Euler angle E1, E2 and E3, KAM, GOS, GROD-Ang, GND Density, Schmid factor)
15	GOS + Grain Boundaries	Define training regions (deformed and recrystallized)	Extract recrystallized fraction Create separate subsets for deformed and recrystallized grains.
16	Repeat 2,3,9-13 for every subset		Re-extract desired (e.g. grain lists)

4. Results

This section presents the EBSD results obtained from the first sample set following consecutive stages of thermal cycling. Starting from Stage 0 to Stage 5, EBSD maps are shown to illustrate the microstructural features characteristic of each corresponding stage.

4.1 Stage 0: As-Reflowed

In Stage 0, the thermal history is limited to the reflow process which is the same for all samples. From the phase map in Figure 19(a), it is observed that β-Sn dominates, as expected. Interfacial IMCs are not indexed at this Stage, the thickness is smaller than the step size used for the bump analysis. Few Cu_6Sn_5 are observed in the bulk. In Figure 19(b), an IPF-colored EBSD map relative to the y-axis of cross-sectioned solder bump is shown. It is evident, that as-reflowed solders in Stage 0 exhibit a dominant beach ball grain morphology while Figure 19(c) reveals, in accordance to the literature, that the orientation of the grains is cyclically twined around [001] axis. Additionally, beach ball grains are separated by HAGBs and in the interior, LAGBs (2-10°) dominate, as shown in Figure 19(d).

Since slip activity plays an important role in microstructure evolution under thermal cycling, the slip activity at Stage 0 is also analyzed to create a baseline. Schmid factor maps provide an overview of the activity of a particular slip system. Tin crystals have 32 slip systems that can be classified in 10 families, listed in Table A2 and Table A3 in the Appendix. One slip system was selected from each family, as shown in, for which the Schmid factor is calculated and mapped. The SF for slip system $(121)[\bar{1}01]$ (SS10) is mapped in Figure 19(e) as an example. Grains colored with darker shades have higher SF values indicating slip activity along the $(121)[\bar{1}01]$system. A SF map for each slip system family is constructed for every sample so that the active slip systems can be identified. The bar plot in Figure 19(f) shows the frequency of slip activity in a Stage 0 sample. SS4 is the most active slip system family in Stage 0.

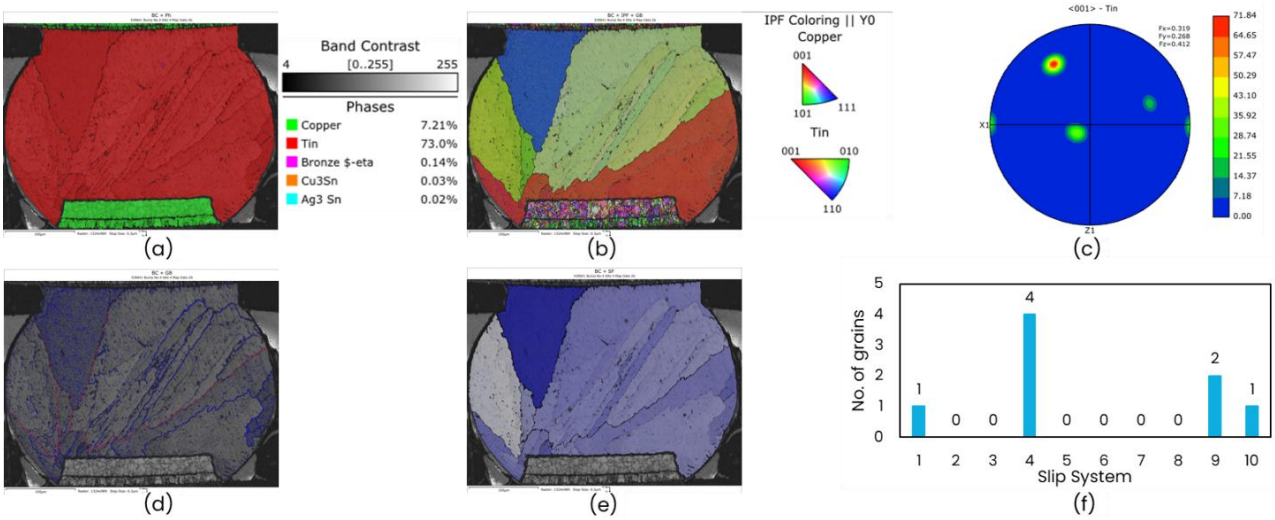

Figure 19: Characterization of solder microstructure at Stage 0. EBSD maps of Sample No.4: (a) Phase map, (b) IPF-colored map relative to y-axis, (c) Pole figure, (d) Grain boundary map. Indicated with blue, green and red are the LAGBs (2-10°), LAGBs (10-15°) and HAGBs, respectively, (e) SF map of SS10 $(121)[\bar{1}01]$, (f) Active slip systems in Stage 0.

4.2 Stage 1, 2 & 3: Recrystallization

Progressive thermal cycling, from Stage 1 to Stage 3, leads to Sn grain refinement as shown in Figure 20. This refinement is indicative of recrystallization, and it is further supported by the absence of orientation gradients in the refined grains. In contrast, larger grains appear discolored, indicating orientation gradients and thus, plastic deformation. Signs of discoloration are marked with yellow arrows in Figure 20. Additionally, based on the IPF-coloring of the grains, it is observed that at Stages 2 and 3, deformed grains show a preferential [110] orientation parallel to the y-axis, while in refined grains, the y-axis is oriented parallel to the [010] direction. These orientations are highlighted by the yellow boxes in Figure 20, each indicating the corresponding preferential orientation. This is also observed in all samples from Stage 2 and 3 shown in Figure A3 in the Appendix.

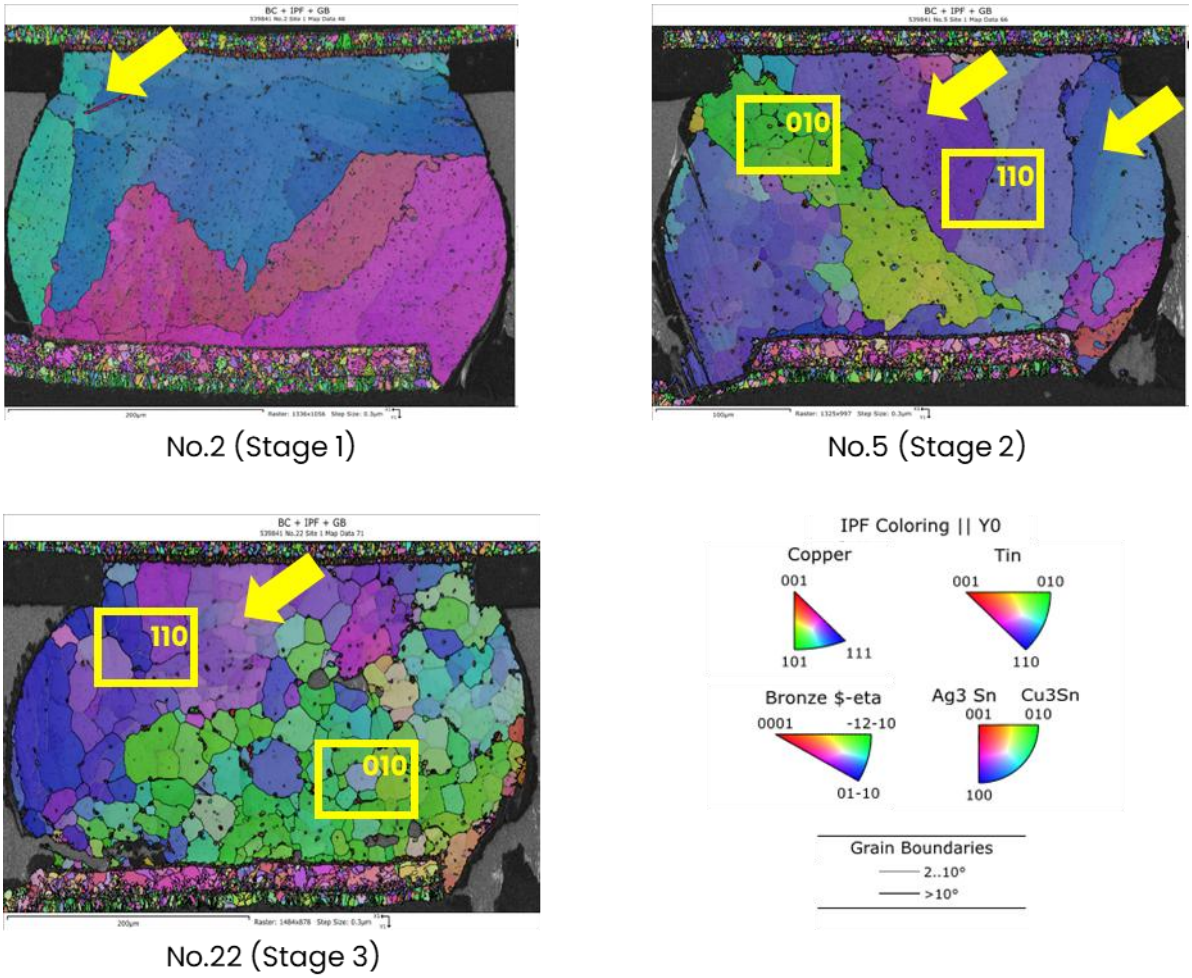

Figure 20: IPF-colored EBSD maps of Stages 1, 2 and 3, respectively.

As thermal cycling progresses, LAGBs gradually transform into HAGBs that surround recrystallized grains. Notably, recrystallized grains, are free of interior LAGBs, indicating the absence of internal stress and thus orientation gradients, which is also evident in the IPF-colored maps. Figure 21(a-c) presents the grain boundary distribution at Stages 1, 2 and 3, respectively. Boundaries in the range of 10-15˚ are plotted separately, as they are considered to be LAGBs(2-10˚) in the process of transitioning into HAGBs. Recrystallized grains are identified through GOS mapping, where they exhibit low values. In Figure 21(d-f),

GOS maps corresponding to Stages 1, 2 and 3 are shown. To exclude grains that were initially small enough to have low GOS values, an additional criterion in the classification of the grains is applied: recrystallized grains must be surrounded by HAGBs. Note that only β-Sn grains are classified. The result of this classification is illustrated in Figure 21(g, i). The complete dataset is available in Figure A4 in the Appendix. Recrystallization is already evident at Stage 1, though only a few recrystallized grains are present. A slight increase is observed at Stage 2, followed by a sharp increase between Stages 2 and 3.

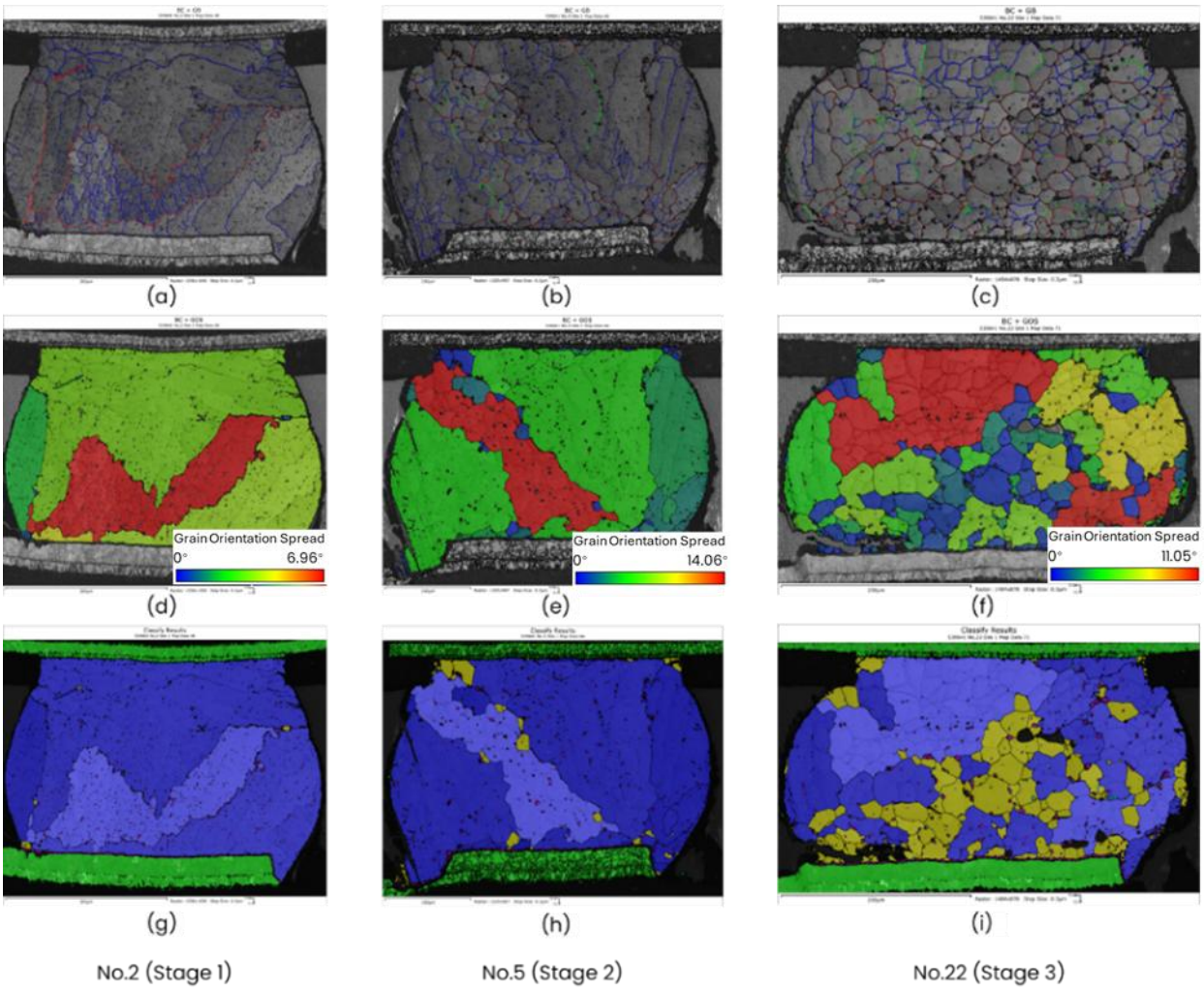

Figure 21: Evolution of: (a-c) Grain boundary distribution. Indicated with blue, green and red are the LAGBs (2-10°), LAGBs (10-15°) and HAGBs, respectively, (d-f) GOS and (g-i) Recrystallized fraction at (a, d, f) Stage 1, (b, e, h) Stage2 and (c, f, i) Stage 3.

The evolution of grain orientation during thermal cycling is monitored through pole figures. From the [001] pole figures, referring to the entire dataset, shown in Figure 22(a, b, c), it is evident that the orientation of c-axis at Stage 1 resembles the Stage 0 orientation with symmetric and well defined poles. At Stage 2, slight broaden peaks are observed, as well as, less intense poles, which is a sign of recrystallization. These phenomena are more pronounced at Stage 3 where poles are less intense and their shape is more spread. Additionally, recrystallized grains show significantly different [001]Sn pole distribution compared to the deformed grains which still dominate the pole distribution of the entire dataset.

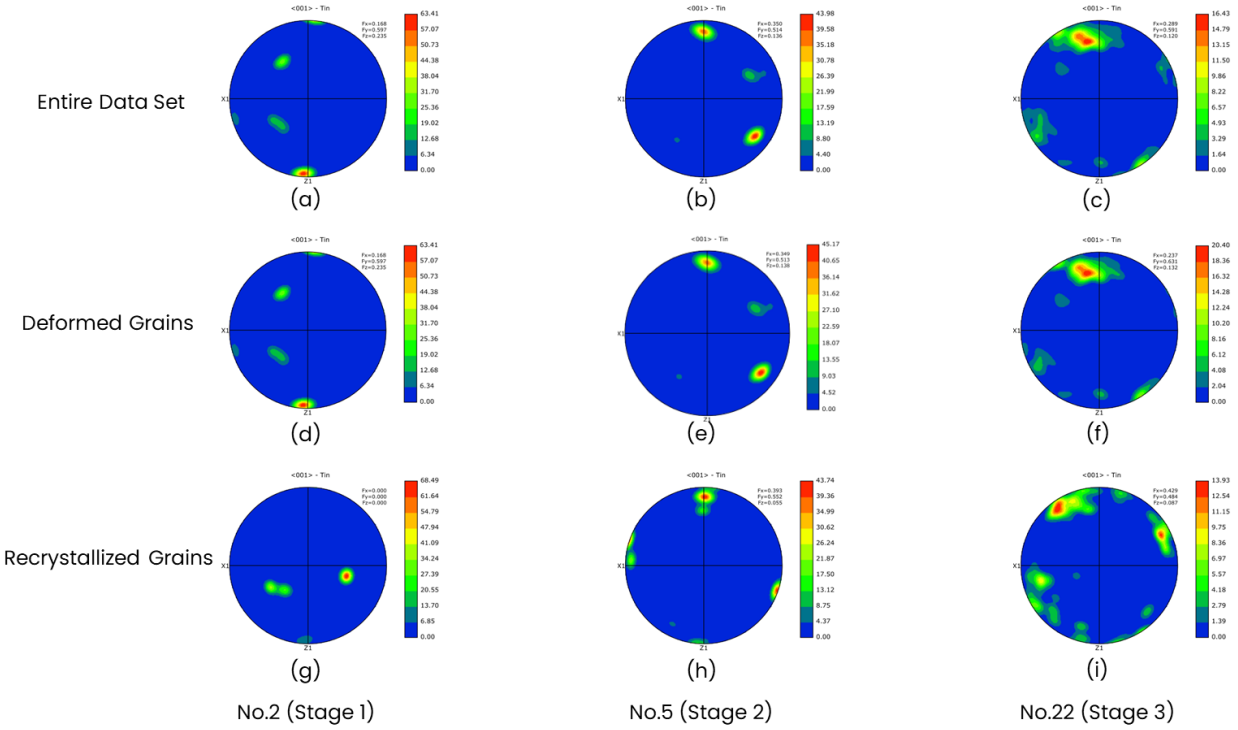

Figure 22: Loss of texture during thermal cycling. Comparison between the entire data set (a, b, c), deformed grains (d, e, f), and recrystallized grains (g, h, i) at Stage 1 (a, d, g), Stage 2 (b, e, h) and Stage 3 (c, f, i). Complete sample set in Figure A5 in the Appendix.

In Figure 23, the overall activity of each slip system at Stage 1, 2 and 3 is presented. Both deformed and recrystallized grains show one dominant active slip system, namely SS10, at Stage 1. It continues to be active as thermal cycling progresses however, the total number of active slip systems increases. At Stage 2, SS10 and SS6 are the most favorable slip systems, while at Stage 3, SS4 becomes the second most favorable slip system after SS10, in both deformed and recrystallized grains.

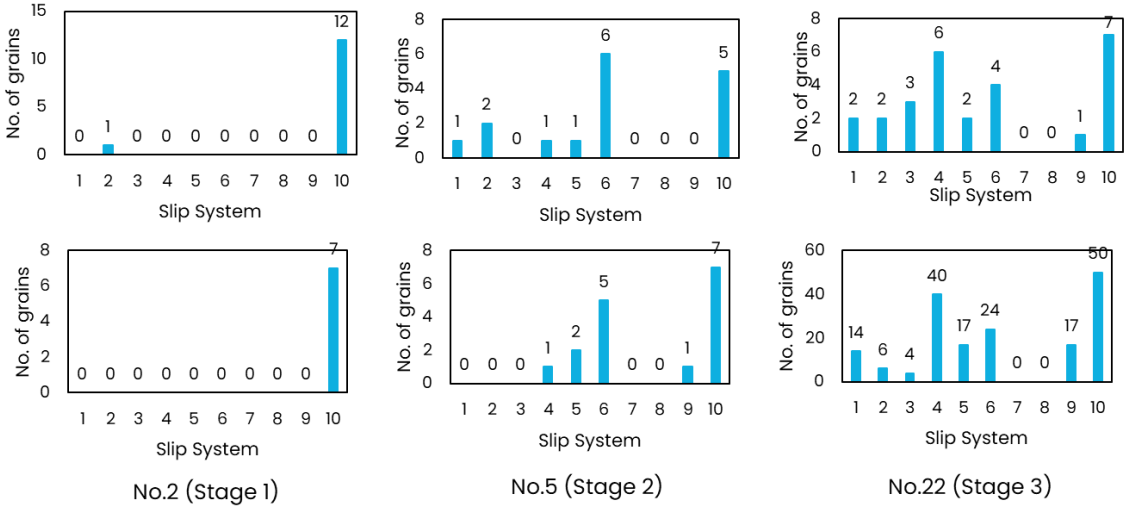

Figure 23: Evolution of slip activity in deformed (top) and recrystallized grains (bottom) at Stages 1, 2 and 3.

4.3 Stage 4 & 5: Crack Initiation & Propagation

In Stage 4 and 5 of thermal cycling, crack initiation and propagation occurs, as shown in Figures 24(a, c). The β-Sn phase still dominates while, the IMCs are coarsened and present at the grain boundaries in the refined region, as indicated by the yellow arrows in Figure 24. Additionally, Cu_6Sn_5 appears as a continuous interfacial layer at the top and bottom side of the solder and compared to Ag_3Sn and Cu_3Sn, Cu_6Sn_5 grains are larger. Although the solders have undergone considerable plastic deformation up to Stage 5, a preferential orientation similar to that observed in Stages 1, 2 and 3 is still evident, as shown in Figure 24(e, g). Specifically, refined grains tend to align their [010] axis with the y-axis, while deformed grains show slight deviation with both the [111] direction becoming increasingly aligned. The recrystallization fraction seems relatively stable between Stages 4 and 5 with recrystallized grains having similar distribution in the matrix, located mostly close to the interfaces where the cracks propagate. The strain state of grains is measured as a function of local misorientation through GROD-Ang and KAM maps, as shown in Figures 24(b,d,f,h). At Stages 4 and 5, following the progression of thermal cycling, strain gradients in the deformed grains appear increased compared to recrystallized grains, which, as expected, are strain free. Moreover, crack initiation is observed in the recrystallized region where it propagates in transgranular manner, parallel to the substrate. Estimation of the Young's modulus considering a loading direction parallel to the y-axis, Figure 24(j, l), reveal decreased values in the recrystallized region. It is also observed that grains with similar orientation exhibit similar modulus values.

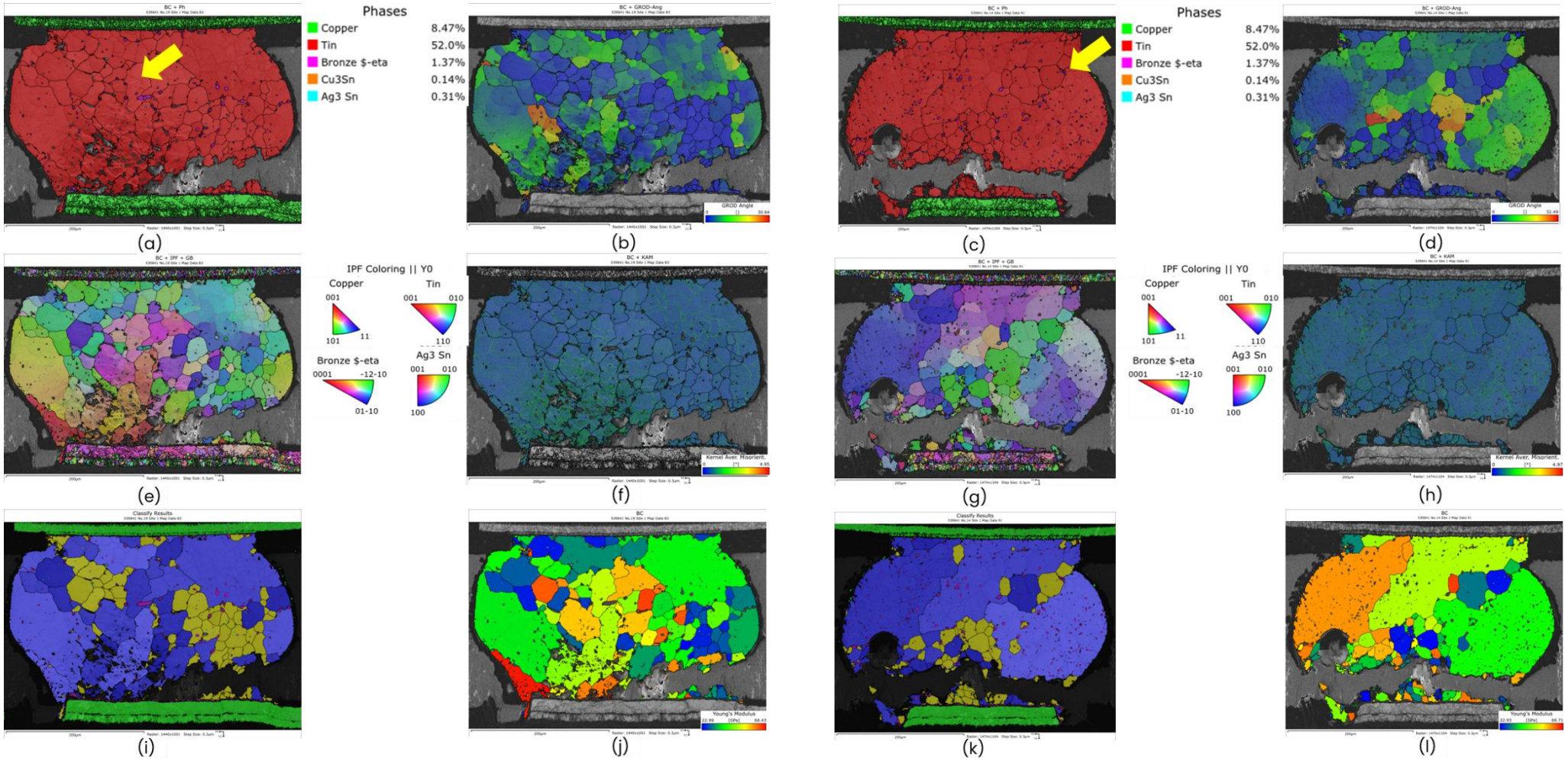

Figure 24: Evolution of: (a,c) Phase distribution, (e, g) IPF-coloring, (i, k) recrystallization fraction, (b, d)GROD, (f, h) KAM and (j, l) Young's Modulus at (a, b, e, f, i, j) Stage 4 and (c, d, g, h, k, l) Stage 5.

5. Discussion

5.1 Microstructure Evolution

Grain Boundaries

While the presence of the Sn matrix and the IMCs is well-established, their distribution can vary significantly between samples, influencing microstructural evolution. From Figure 19(a) and Figure 24(a) it is observed that throughout all stages of thermal cycling, the Sn matrix is dominant, and therefore parameters can be analyzed with respect to Sn properties. In addition to phase distribution, grain boundaries are closely tied to microstructural evolution and the thermomechanical response of solders. In this context, the overall evolution of grain boundary types over time is illustrated in Figure 25. LAGBs to HAGBs transformation occurs during the first three stages of thermal cycling, resulting in a reduction of approximately 40% in LAGBs(2-10˚) and a 20% increase in HAGBs. After the third stage, the grain boundary distribution remains relatively stable for all types.

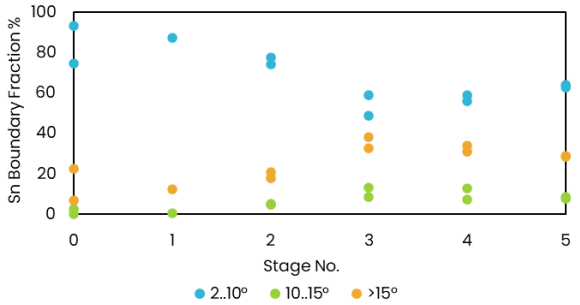

Figure 25: Evolution of grain boundary distribution over time

Recrystallization and Grain Size

The increase in HAGBs and the significant grain refinement observed during thermal cycling are indicative of recrystallization and are further supported by the fact that the newly formed grains are free of orientation gradients and are surrounded by HAGBs. The lack of orientation gradients is attributed to low misorientation and the absence of internal strains indicating low dislocation content. Recrystallization fraction is calculated based on the GOS approach, discussed in the previous section, and its evolution over time is illustrated in Figure 26. During the initial stages of thermal cycling, the fraction increases at a slow rate without exceeding 3%. Between stages two and three, the fraction increases significantly to approximately 22% where it remains relatively constant.

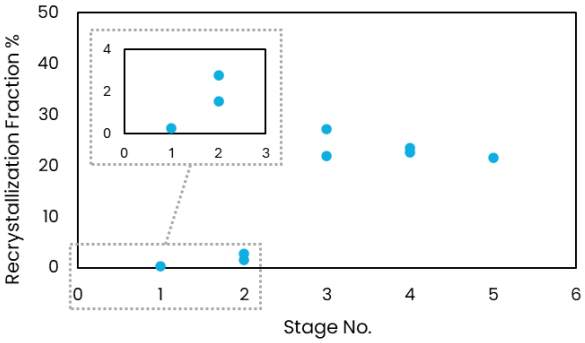

Figure 26: Evolution of recrystallization fraction during thermal cycling

Grain size is quantified using the area-weighted mean grain size because larger grains have a greater impact on the microstructure and the properties of the material. The evolution of the Sn grain size is examined separately for deformed and recrystallized grains, as shown in Figure 27, for more accurate assessment of microstructural changes during thermal cycling. Deformed grains exhibit larger grains during all stages of thermal cycling, ranging from 70 to 180 μm. Their size has a downward trend while the scattering of the values increases at intermediate stages. Recrystallized grains are formed after the first stage and their size keeps increasing until the third stage where it reaches a plateau of approximately 22 μm.

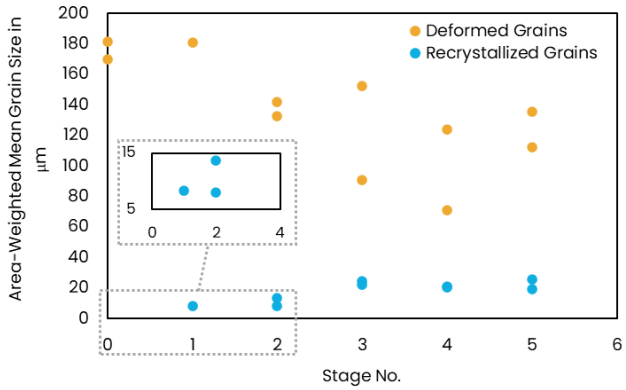

Figure 27: Evolution of Sn deformed and recrystallized grain size during thermal cycling.

The trends revealed in Figures 25, 26 and 27 are strong indicators of primary and continuous dynamic recrystallization occurring [94, 95]. More precisely, primary recrystallization occurs in rotated regions where shear deformation is high, through dislocation absorption across already-existing HAGBs. This is evident in Figure 28, where newly formed recrystallized grains are located at already-existing HAGBs, as indicated by the yellow arrows.

In continuous dynamic recrystallization, dislocations are absorbed by subgrain boundaries leading to grain refinement and the formation of HAGBs, typically in high strain regions close to interfaces and cracks. Such regions are marked with yellow arrows in Figure 29. Moreover, the grain size stabilizes due to dynamic equilibrium between dislocation generation and recovery [94, 95]. Therefore, deformation continues without significant changes in the microstructure, in contrast to primary recrystallization that goes on until the Sn matrix is consumed. In Figure 25, dynamic recrystallization is evident from the grain size stabilization and it can be concluded that it is more dominant since there is no significant spread of the values in the stabilized region.

Additionally, in Figure 29 it is observed, and highlighted in yellow boxes, that recrystallized grains in the bulk appear slightly larger with no orientation gradients while, recrystallized grains close to cracks and interfaces, are finer with slightly larger misorientation. The difference in size and misorientation is attributed to the different recrystallization mechanisms. Dynamic recrystallization occurs during ongoing deformation, and thus, slight misorientation is expected. In primary recrystallization the grains are new and strain free therefore no misorientation is observed. Regarding the grain size, in primary recrystallization it gradually increases while in dynamic, grain growth stops when the dynamic equilibrium is reached.

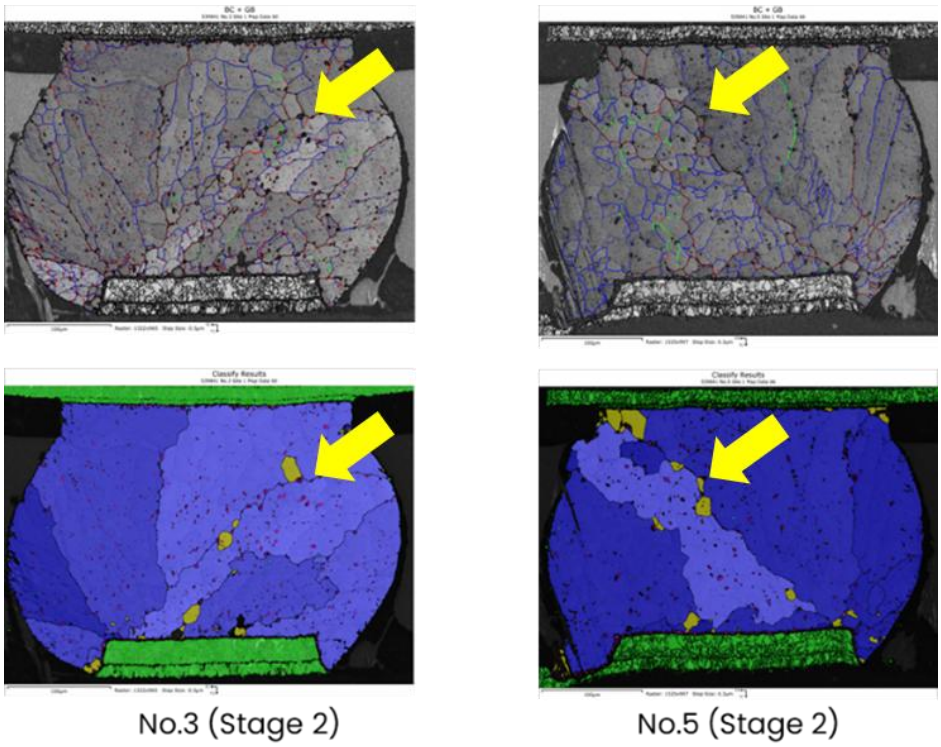

Figure 28: Primary recrystallization evident at the early stages of thermal cycling. Grain boundary (top) and recrystallization (bottom) maps for Sample No 3 & 5 of Stage 2

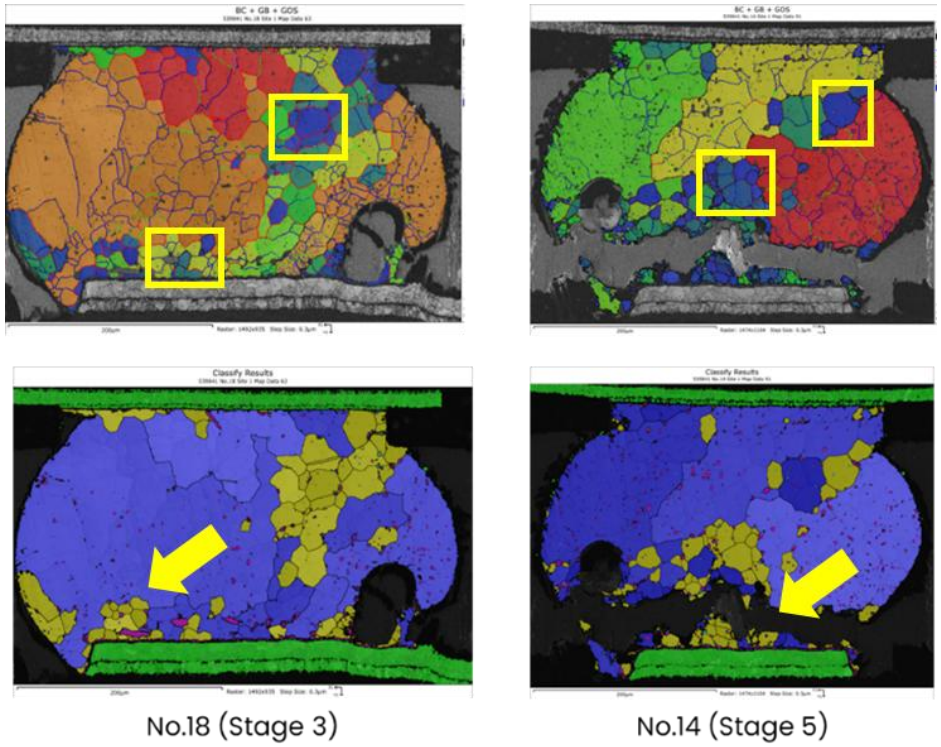

Figure 29: Differentiation between recrystallized grains resulting from primary and continuous dynamic recrystallization. GOS overlayed by grain boundaries (top) and recrystallization (bottom) maps of Sample No.18 (Stage 3) and No.14 (Stage 5).

Moreover, from Figures 26 and 27, it can be derived that recrystallization occurs between Stage 1 and Stage 3. Given that both the recrystallization fraction and recrystallized grain size stabilizes after Stage 3 due to the dominance of dynamic recrystallization, it is assumed that the solder will keep deforming with thermal cycling but without experiencing changes in the microstructure. Considering the increase in HAGBs due to recrystallization and their susceptibility to intergranular cracking, the fatigue life of solders depends on crack propagation once recrystallization initiates.

During thermal cycling, change in orientation is expected. Figure 30 shows the average angle between [001]Sn and the substrate over time for deformed and recrystallized grains, while measurements from Stage 0 samples (No.4 and No.8) are included as a point of reference. It is observed in deformed grains that the orientation of [001]Sn gradually shifts closer to the substrate. In contrast, recrystallized grains exhibit similar orientations to the initial, after the first stage of thermal cycling. However, from the second stage onwards, the orientation shifts sharply, by 20°, towards the substrate, where it remains relatively stable. This indicates that the c-axis shifts towards the direction parallel to the substrate as thermal cycling progresses. In the literature, [001]Sn parallel to the substrate is considered the most detrimental orientation for the solder reliability [20, 39, 40]. Considering the directionality of CTE and Young's modulus in accordance with Figure 6, SAC solders are stiffer and have the high CTE along the [001] direction causing internal stress. Therefore, the fact that the first cracks are observed after the third stage might be attributed to the [001]Sn orientation.

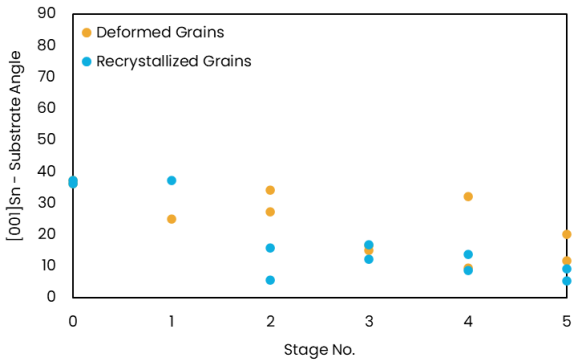

Figure 30: Evolution of [001]Sn - substrate angle

The rotation of [001]Sn towards the direction parallel to the substrate indicates preferential slip activation. In Figure 31, the overall activity of each slip system at stages 1, 2 and 3 is presented. Both deformed and recrystallized grains show increased activity of the slip systems SS4, SS6, and SS10, as illustrated in Figure 32. An examination of the bar plots representing the slip activity for deformed and recrystallized grains in each sample (Figures A6 and A7 in the Appendix) shows that, in most samples, the same three slip systems are active as thermal cycling progresses.

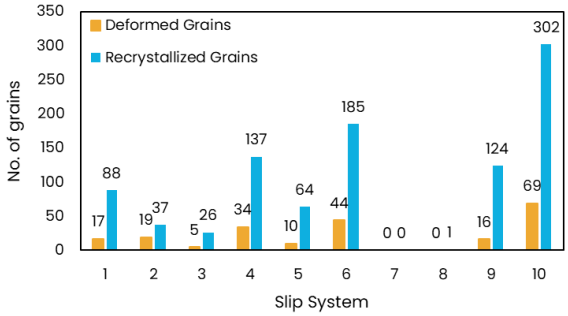

Figure 31: Overall slip activity in deformed and recrystallized grains.

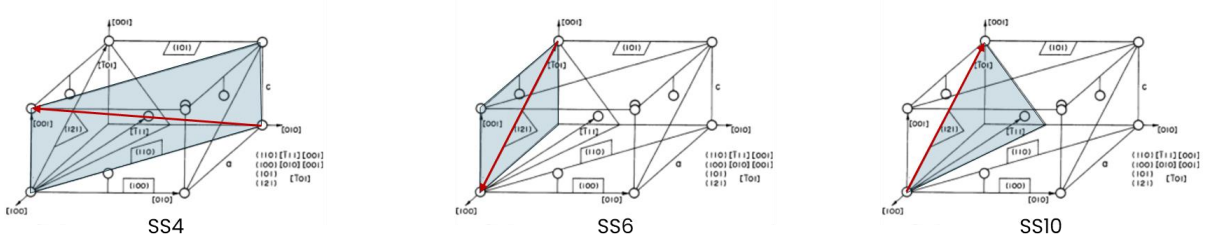

SS4 (110)[1$\bar{1}$1] SS6 (010)[10$\bar{1}$] SS10 (121)[$\bar{1}$01]

Figure 32: Schematic illustration of slip systems SS4, SS6 and SS10

There is no obvious reason why these particular slip systems are active. Notably, SS6 shares the same slip direction with SS10. The {110} slip planes in SS4 have the largest interplanar distance, while <111> directions are some of the most densely packed directions, allowing for easier dislocation glide. This uniform behavior is unexpected considering the fact that individual bumps with different microstructures were tested. In Figures A6 and A7 in the Appendix it is revealed that SS4 is already activated at Stage 0, therefore, it is possible that the thermal history during reflow, promoted textures that favor the activation of this slip system. Given the tendency of grains to rotate so that they bring their [001]Sn parallel to the substrate, it can be assumed that by controlling the reflow process it may be possible to predefine the initial microstructure and, based on orientation-dependent parameters, prevent, delay or even predict solder joint failure.

Such a parameter apart from slip activity, is the Young's Modulus. Although accurate monitoring of mechanical property evolution requires experimental validation, EBSD can provide a reasonable first approximation. In this regard, Young's Modulus EBSD maps are constructed considering a loading direction parallel to the y-axis, maps of the entire sample set can be found in Figure A8 in the Appendix. Grains with similar orientation demonstrate similar modulus values. As thermal cycling progresses, Young's Modulus decreases. Figure 33 illustrates the evolution of the modulus during thermal cycling in deformed and recrystallized grains. Recrystallized grains typically exhibit slightly lower values and this can be possibly attributed to the fact that recrystallized grains in a given sample have more active slip systems compared to deformed grains, as shown in Figures A6 and A7 in the Appendix. This enables them to accommodate more easily plastic deformation although the HAGBs between the grains are prone to crack initiation.

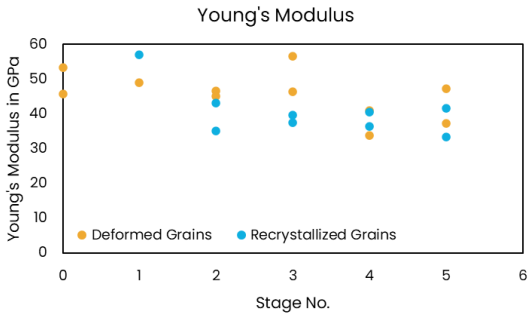

Figure 33: Evolution of Young's Modulus in deformed and recrystallized grains over time

As previously mentioned, solder fatigue life depends on crack propagation once recrystallization occurs. Crack propagation is affected by the evolution of IMCs. When they are fine and dispersed in the matrix,

like in the first stages of thermal cycling, they have greater capability to act as barriers to dislocation motion by dislocation and grain boundary pinning. This process prevents the formation of high-angle grain boundaries and thus, recrystallized grains [40, 59]. This can possibly explain the small size and number of recrystallized grains appearing after the first stage of thermal cycling. In Figure 34, the evolution of IMC grain size and number density is illustrated. Ag_3Sn and Cu_3Sn follow a similar upward trend while Cu_6Sn_5 shows an increase with thermal cycling but exhibits larger scattering at intermediate stages compared to the other IMCs. This is possibly attributed to indexing of Cu_6Sn_5 grains at the interfacial layers at later stages of thermal cycling, where those layers grow thicker and grains are larger.

The gradual increase in grain size and number density is accompanied by increase in the recrystallization fraction (Figure 26), indicating grain boundary unpinning and thus a higher risk for crack initiation and propagation considering also the susceptibility of HAGBs to intergranular cracking. IMCs have very few slip systems, and this makes it difficult to accommodate deformation therefore they become more brittle and may act as crack initiation points.

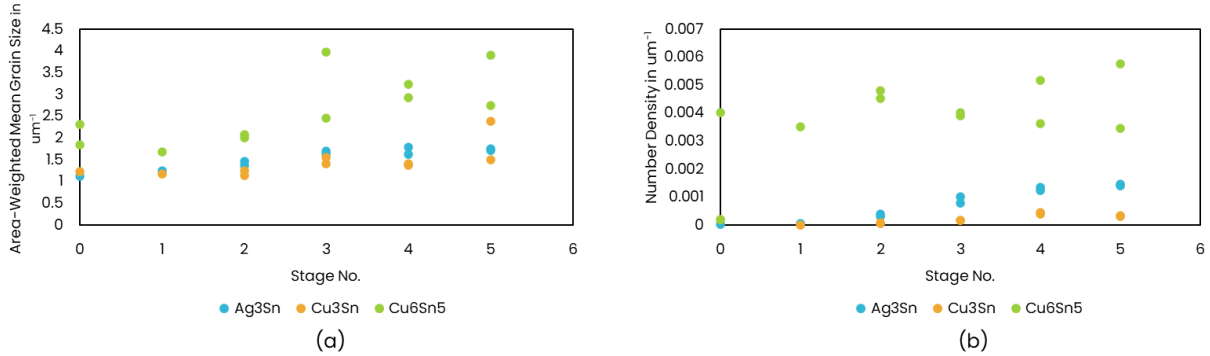

Figure 34: Evolution of IMC (a) size and (b) number density during thermal cycling

In the literature coarsening of IMCs is usually attributed to the Ostwald ripening effect where small grains are "consumed" and incorporated into larger grains [5]. In this case, a decrease in the grain boundaries and the number density of the IMCs would be observed as the grains would be fewer and larger. On the contrary, an increase in the grain boundary fraction is observed for all IMCs, in Figure 35, while the number density in Figure 34(b) exhibits a similar trend. Therefore, the dominant growth mechanism of IMCs is not Ostwald ripening and is likely related to atomic or grain boundary diffusion effects, although this was not further verified.

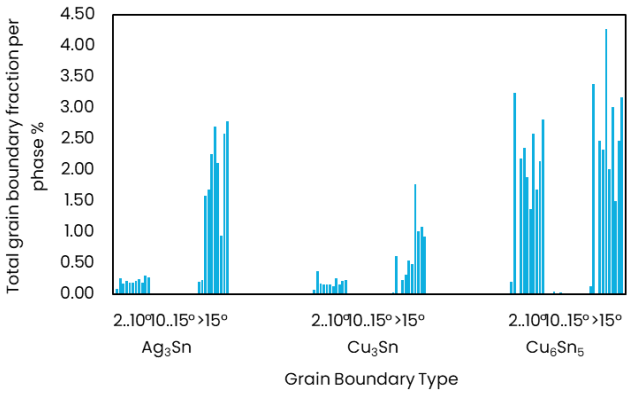

Figure 35: IMC grain boundary fraction. In each cluster the Stage No. increases from left to right

5.2 Limitations

Dependence on Step Size

Further research is required for better understanding of the mechanisms behind IMC coarsening. In the present work, the main limitation in the study of IMCs was the EBSD step size. More focus was given in the study of the overall microstructure of the solder and for that, the optimum step size amounted to 0.3 um, which is considerably higher than the average IMC grain size and for this reason, a lot of IMCs either in the form of precipitates or interfacial layers were not indexed. Separate scans with smaller step sizes could potentially provide more information, however, consistency in experimental conditions would be compromised. Additionally, it is the author's belief that IMC-related phenomena, such as coarsening, voiding or cracking, are more complex than initially expected and are worth a dedicated study out of the scope of the present study.

Bridging EBSD and Predictive Modeling: Stored Energy Approach

In the context of exploring the capabilities of EBSD, aiming for efficient ways perform the analysis based on data that can be easily fed into a model, GND density and Stored energy density were calculated. Although the resolution of EBSD does not allow for dislocation detection, a rough approximation of the GND density can be calculated based on KAM values. Using a threshold of 5°, the contribution of grain boundaries in the misorientation can be excluded. In Figure 36, the obtained GND density of deformed and recrystallized grains is presented. Deformed grains although they were expected to have higher GND density, show similar values and trends with the recrystallized grains. As thermal cycling progresses, the density decreases until the third stage, where the trend is reversed.

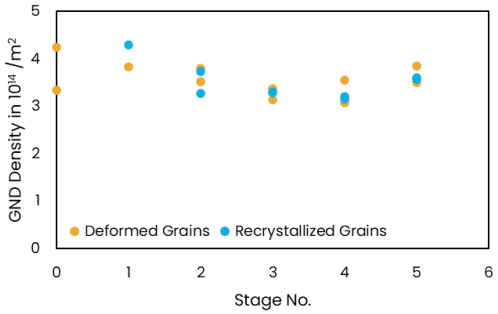

Figure 36: GND density evolution during thermal cycling

Stored Energy Density is calculated based on the obtained values of GND density in accordance with Equation E5. The shear modulus is estimated through EBSD in the same way as the Young's modulus. The x-axis along the XZ-plane is considered to be the shear direction while the Burger's vector is set parallel to the [001] direction because it is the smallest lattice translation vector between two equilibrium positions in Sn crystals. Illustrated in Figure 37 is the SED for the total amount of grains as well as for deformed and recrystallized grains. The overall trend is similar to the GND density with a larger scattering of the values. Deformed grains have approximately 8.5% higher SED compared to recrystallized grains.

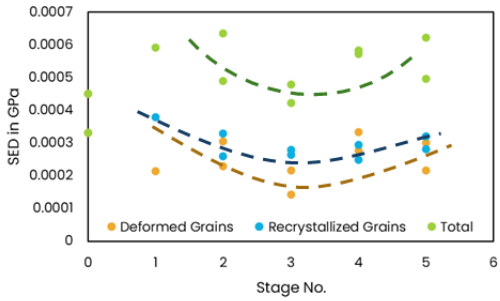

Figure 37: Estimated values of SED during thermal cycling. Trend lines were manually drawn as approximations.

The downward trend observed in Figure 37 could be explained by the dislocation annihilation and absorption by the LAGBs during recrystallization up until the third stage. This argument is in agreement with observations in the recrystallization fraction and grain boundary evolution where they also experience a shift in their trend at the third stage, reaching a plateau. From stage three onwards, since recrystallization is no longer occurring and dislocations are not "consumed" by LAGBs, they can only accumulate at the surface, pile up at the grain boundaries, and increase their density. Therefore, the observed trend seems to have physical meaning at least for the deformed grains. The unexpectedly high dislocation density in the recrystallized grains may be attributed to methodological limitations in the current approach.

Although KAM is a pixel property, GND density is automatically calculated per grain. Perhaps, calculation of the GND density per pixel could provide more accurate and localized values. Additionally, the fact that KAM is sensitive to the step size is concerning, introduces variability and therefore, the absolute values may not be reliable and should be interpreted with caution. Subsequently, this approach is more suitable if the desired result is an indication of a trend rather than absolute values. In the present case the trend of both GND and SED seems to have physical meaning, therefore the trend could still be used theoretically. However, there is no validation of the result, and the deviation from SED calculations obtained from strain formulas is not known.

In-Situ Experiments: Pre-Cross Sectioned Solders

Finally, two sets of samples were prepared yet only the first one was presented in the results. The second approach was that solders would enter the thermal cycling chamber already cross-sectioned and monitor the evolution of the microstructure of the same solder. In reality, no significant changes were observed in the microstructure. In Figure 38, IPF-colored and grain boundary maps of sample No.4 during consecutive stages of thermal cycling are shown. It is observed that after three stages there is no significant change in the orientation of Sn crystals nor in the size of the grains. Orientation gradients are absent in the majority of the indexed surface indicating that recrystallization does not occur. Similarly, the grain boundary distribution remains relatively stable except for a slight reduction in LAGBs. Grain

boundaries between 10 and 15 degrees are not detected indicating that LAGBs are not in the process of transitioning to HAGBs and therefore supporting the argument that recrystallization does not occur.

This is attributed to the free cross-sectioned surface from which the applied thermal stress releases in the form of surface roughness. If the samples were embedded and somehow more constrained in space, it may have resulted in evolution of the microstructure or even more rough surface. Still, considering that these samples come from reliability tests, embedded samples would not serve the intended purpose because tests need to be conducted as close to the service conditions as possible. Although this set of experiments was not successful, important remarks were made. First, pre-cross-sectioned solders are not a suitable approach for this kind of analysis, and second, in-situ studies do not always guarantee better results.

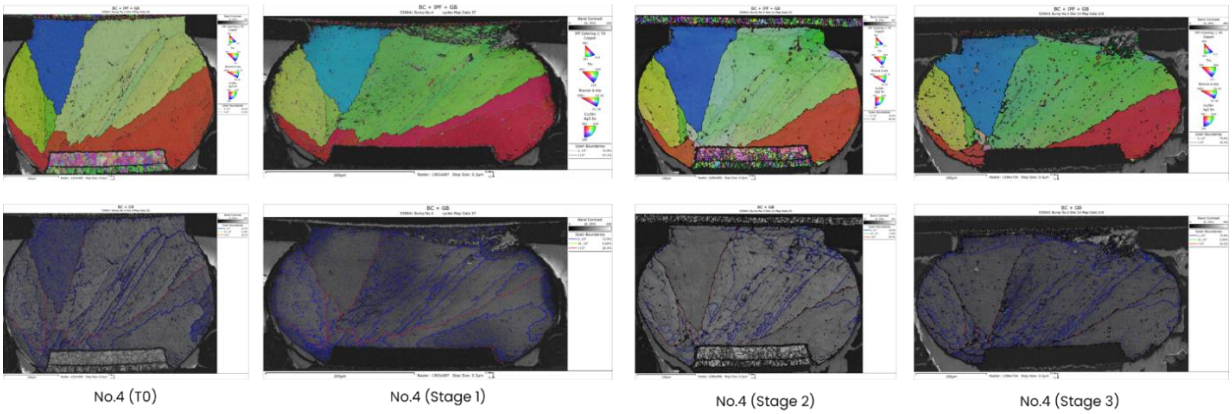

Figure 38: Evolution of microstructure and grain boundary distribution during thermal cycling of pre-cross-sectioned sample No.4

6. Conclusions and Outlook

This work provides and in depth study of the microstructure evolution in SAC solders during thermal cycling using EBSD. More emphasis was placed on microstructural features such as recrystallization and slip activity, that act as drivers in deformation and failure mechanisms.

Thermal cycling is the primary cause of solder joint cracking in failures of electronic devices in service conditions. It is proven to cause microstructural changes leading to failure however, these are rarely investigated. Therefore, the motivation behind this project was to shed light on the overall evolution of the microstructure.

Two distinct recrystallization mechanisms were identified; primary and continuous dynamic with the former appearing along HAGBs in the bulk of the solder and the latter in the form of fine grains close to interfaces and cracks. Recrystallization was found to occur between Stage 1 and Stage 3, after which it stabilizes. This is attributed to the continuous dynamic recrystallization mechanism which seems to be the dominating mechanism of the two. Once recrystallization is stabilized fatigue life depends entirely on crack propagation.

A consistent trend was observed across all samples, where grains rotate in such way that their [001]Sn direction will align parallel to the substrate. Additionally, slip systems 4, 6 and 10 are identified as the most active ones across all solders in all stages. This indicates that slip activity is linked to the initial orientation established by reflow and based on that, the slip systems that will accommodate rotation towards the minimum [001]Sn-Substrate angle, will be activated.

IMC coarsening is evident during thermal cycling, as well as the unpinning of grain boundaries however, the selected step size was too large to delve into their role in solder joint degradation. A decrease in Young's modulus is observed in recrystallized grains probably attributed to the higher amount of active slip systems compared to deformed grains.

Attempts to link EBSD-derived parameters such as GND and Stored Energy Density with numerical models proved to be more challenging than initially expected. More robust methods to obtain these parameters are needed as well as simulation inputs to estimate the deviation.

Lastly, the use of pre-cross-sectioned solders is not suitable for this type of analysis and reliability tests under service conditions. The ability to capture deformation mechanisms is limited due to thermal stress relaxation through the free surface.

References

[1] M. Judd and K. Brindley, "Soldering process," in *Soldering in Electronics Assembly (Second Edition)*, Elsevier BV, 1999, pp. 1–22. doi: https://doi.org/10.1016/b978-075063545-5/50003-0.

[2] H.-M. Tong, Y.-S. Lai, and C. P. Wong, *Advanced Flip Chip Packaging*. Springer Nature, 2013. doi: https://doi.org/10.1007/978-1-4419-5768-9.

[3] S. Cheng, C.-M. Huang, and M. Pecht, "A review of lead-free solders for electronics applications," *Microelectronics Reliability*, vol. 75, pp. 77–95, Aug. 2017, doi: https://doi.org/10.1016/j.microrel.2017.06.016.

[4] S. H. Hu *et al.*, "Effects of bismuth additions on mechanical property and microstructure of SAC-Bi solder joint under current stressing," *Microelectronics Reliability*, vol. 117, pp. 114041–114041, 2021, doi: https://doi.org/10.1016/j.microrel.2021.114041.

[5] R. J. Coyle, K. Sweatman, and B. Arfaei, "Thermal Fatigue Evaluation of Pb-Free Solder Joints: Results, Lessons Learned, and Future Trends," *JOM: The Journal of The Minerals, Metals & Materials Society (TMS))*, vol. 67, no. 10, pp. 2394–2415, 2015, doi: https://doi.org/10.1007/s11837-015-1595-1.

[6] T. Alander, S. Nurmi, P. Heino, and E. Ristolainen, "Impact of component placement in solder joint reliability," *Microelectronics Reliability*, vol. 42, no. 3, pp. 399–406, 2002, doi: https://doi.org/10.1016/s0026-2714(01)00217-7.

[7] M. A. Matin, W. P. Vellinga, and M. G. D. Geers, "Thermomechanical fatigue damage evolution in SAC solder joints," *Materials Science and Engineering: A*, vol. 445–446, pp. 73–85, 2007, doi: https://doi.org/10.1016/j.msea.2006.09.037.

[8] B. Zhou, "Characterization of tin crystal orientation evolution during thermal cycling in lead-free solder joints," PhD Dissertation, Michigan State University, 2012.

[9] K. Sweatman *et al.*, "iNEMI Pb-Free Alloy Characterization Project Report: Part III - Thermal Fatigue Results for Low - Ag Alloys," International Electronics Manufacturing Initiative (iNEMI) , 2012.

[10] R. Coyle *et al.*, "Thermal Cycling Reliability and Failure Mode of two Ball Grid Array Packages with High Reliability Pb-Free Solder Alloys," in *Proceedings of SMTA International*, Rosemont, Illinois, USA.: Surface Mount Technology Association (SMTA), 2019.

[11] E. George, M. Osterman, M. Pecht, R. Coyle, R. Parker, and E. Benedetto, "Thermal Cycling Reliability of Alternative Low-Silver Tin-based Solders," *International Symposium on Microelectronics*, vol. 2013, no. 1, pp. 120–127, 2013, doi: https://doi.org/10.4071/isom-2013-ta45.

[12] M. Rebosolan, M. van Soestbergen, J. J. M. Zaal, T. Hauck, A. Dasgupta, and B. Chen, "Effect of microstructural variability on fatigue simulations of solder joints," *Microelectronics Reliability*, vol. 162, p. 115511, 2024, doi: https://doi.org/10.1016/j.microrel.2024.115511.

[13] K. C. Otiaba, R. S. Bhatti, N. N. Ekere, S. Mallik, and M. Ekpu, "Finite element analysis of the effect of silver content for Sn–Ag–Cu alloy compositions on thermal cycling reliability of solder die attach," *Engineering Failure Analysis*, vol. 28, pp. 192–207, 2013, doi: https://doi.org/10.1016/j.engfailanal.2012.10.008.

[14] J. Depiver, S. Mallik, and E. H. Amalu, "Comparative Analysis of SAC Solder Alloys for Enhanced Reliability in Electronic Assemblies: A Finite Element Approach," *Research Square*, 2024, doi: https://doi.org/10.21203/rs.3.rs-4755675/v1.

[15] K. N. Reeve, J. R. Holaday, S. Choquette, I. E. Anderson, and C. A. Handwerker, "Advances in Pb-free Solder Microstructure Control and Interconnect Design," *Journal of Phase Equilibria and Diffusion*, vol. 37, no. 4, pp. 369–386, 2016, doi: https://doi.org/10.1007/s11669-016-0476-9.

[16] J. Wu, S. Xue, J. Wang, S. Liu, Y. Han, and L. Wang, "Recent progress of Sn–Ag–Cu lead-free solders bearing alloy elements and nanoparticles in electronic packaging," *Journal of Materials Science*

Materials in Electronics, vol. 27, no. 12, pp. 12729–12763, 2016, doi: https://doi.org/10.1007/s10854-016-5407-3.

[17] L. Gao *et al.*, "Effect of alloying elements on properties and microstructures of SnAgCu solders," *Microelectronic Engineering*, vol. 87, no. 11, pp. 2025–2034, 2010, doi: https://doi.org/10.1016/j.mee.2010.04.007.

[18] L. Sun and L. Zhang, "Properties and Microstructures of Sn-Ag-Cu-X Lead-Free Solder Joints in Electronic Packaging," *Advances in Materials Science and Engineering*, vol. 2015, pp. 1–16, 2015, doi: https://doi.org/10.1155/2015/639028.

[19] S.-M. Kang, P. A. Lauro, D.-Y. Shih, D. J. Henderson, and K. J. Puttlitz, "Microstructure and mechanical properties of lead-free solders and solder joints used in microelectronic applications," IBM Journal of Research and Development, vol. 49, no. 4.5, pp. 607–620, 2005, doi: https://doi.org/10.1147/rd.494.0607.

[20] H. Chen, B. Yan, M. Yang, X. Ma, and M. Li, "Effect of grain orientation on mechanical properties and thermomechanical response of Sn-based solder interconnects," Materials Characterization, vol. 85, pp. 64–72, 2013, doi: https://doi.org/10.1016/j.matchar.2013.07.004.

[21] L. P. Lehman, Y. Xing, T. R. Bieler, and E. J. Cotts, "Cyclic twin nucleation in tin-based solder alloys," *Acta Materialia*, vol. 58, no. 10, pp. 3546–3556, 2010, doi: https://doi.org/10.1016/j.actamat.2010.01.030.

[22] B. Arfaei, F. Mutuku, R. Coyle, E. Cotts, and J. Wilcox, "Failure mechanism and microstructural evolution of Pb-free solder alloys in thermal cycling tests: Effect of solder composition and Sn grain morphology," *2015 IEEE 65th Electronic Components and Technology Conference (ECTC)*, pp. 118–126, 2015, doi: https://doi.org/10.1109/ectc.2015.7159580.

[23] B. Arfaei *et al.*, "Reliability and failure mechanism of solder joints in thermal cycling tests," in *2013 IEEE 63rd Electronic Components and Technology Conference*, IEEE, 2013. doi: https://doi.org/10.1109/ectc.2013.6575693.

[24] B. Arfaei, N. Kim, and E. J. Cotts, "Dependence of Sn Grain Morphology of Sn-Ag-Cu Solder on Solidification Temperature," *Journal of Electronic Materials*, vol. 41, no. 2, pp. 362–374, 2011, doi: https://doi.org/10.1007/s11664-011-1756-0.

[25] J. W. Xian, Y. L. Xu, S. Stoyanov, R. J. Coyle, F. P. E. Dunne, and C. M. Gourlay, "The role of microstructure in the thermal fatigue of solder joints," *Nature Communications*, vol. 15, no. 1, 2024, doi: https://doi.org/10.1038/s41467-024-48532-6.

[26] D. Mondal, M. A. Haq, J. C. Suhling, and P. Lall, "Effects of β-Sn Crystal Orientation on the Deformation Behavior of SAC305 Solder Joints," in *2022 IEEE 72nd Electronic Components and Technology Conference (ECTC)*, IEEE, 2022, pp. 1658–1667. doi: https://doi.org/10.1109/ectc51906.2022.00262.

[27] T. Laurila, V. Vuorinen, and J. K. Kivilahti, "Interfacial reactions between lead-free solders and common base materials," *Materials Science and Engineering: R: Reports*, vol. 49, no. 1–2, pp. 1–60, 2005, doi: https://doi.org/10.1016/j.mser.2005.03.001.

[28] S. Kumar and J. Jung, "Mechanical and electronic properties of Ag3Sn intermetallic compound in lead free solders using ab initio atomistic calculation," *Materials science and engineering. B*, vol. 178, no. 1, pp. 10–21, 2013, doi: https://doi.org/10.1016/j.mseb.2012.10.003.

[29] Q. Zhang, "Investigations on Microstructure and Mechanical Properties of the Cu/Pb-free Solder Joint Interfaces," PhD Dissertation, Springer Nature, University of Chinese Academy of Sciences, Beijing, China, 2015. doi: https://doi.org/10.1007/978-3-662-48823-2.

[30] S. Fürtauer, D. Li, D. Cupid, and H. Flandorfer, "The Cu–Sn phase diagram, Part I: New experimental results," *Intermetallics*, vol. 34, pp. 142–147, 2013, doi: https://doi.org/10.1016/j.intermet.2012.10.004.

[31] A. M. Gusak, K. N. Tu, and C. Chen, "Extremely rapid grain growth in scallop-type Cu6Sn5 during solid–liquid interdiffusion reactions in micro-bump solder joints," *Scripta Materialia*, vol. 179, pp. 45–48, 2020, doi: https://doi.org/10.1016/j.scriptamat.2020.01.005.

[32] M. Ghaleeh, A. Baroutaji, N. Al-Esawi, S. Rasool, and T. Chaudhary, "Creep properties of environmentally friendly lead-free SAC solder in ball grid array solder connection subjected to cyclic loading," *Sustainable & Green Materials*, 2025, doi: https://doi.org/10.1080/29965292.2025.2529292.

[33] T.-K. Lee, B. Zhou, L. Blair, K.-C. Liu, and T. R. Bieler, "Sn-Ag-Cu Solder Joint Microstructure and Orientation Evolution as a Function of Position and Thermal Cycles in Ball Grid Arrays Using Orientation Imaging Microscopy," *Journal of Electronic Materials*, vol. 39, no. 12, pp. 2588–2597, 2010, doi: https://doi.org/10.1007/s11664-010-1348-4.

[34] J. Han *et al.*, "Study on morphology and interface relationship between Ag3(Sn, In) and Cu6(Sn, In)5," *Materials Chemistry and Physics*, vol. 297, pp. 127402–127402, 2023, doi: https://doi.org/10.1016/j.matchemphys.2023.127402.

[35] G. Yang, X. Li, E. Ren, and S. Li, "Morphology evolution and grain orientations of intermetallic compounds during the formation of full Cu3Sn joint," *Intermetallics*, vol. 145, pp. 107555–107555, 2022, doi: https://doi.org/10.1016/j.intermet.2022.107555.

[36] K. Nogita, C. M. Gourlay, S. D. McDonald, Y. Q. Wu, J. Read, and Q. F. Gu, "Kinetics of the η–η′ transformation in Cu6Sn5," *Scripta Materialia*, vol. 65, no. 10, pp. 922–925, 2011, doi: https://doi.org/10.1016/j.scriptamat.2011.07.058.

[37] F. Somidin *et al.*, "Inhibition of cracking in Cu_6Sn_5 intermetallic compounds at the interface of lead-free solder joint by controlling the reflow cooling conditions," in *2019 International Conference on Electronics Packaging (ICEP)*, 2019, pp. 223–228. doi: https://doi.org/10.23919/icep.2019.8733594.

[38] T. R. Bieler, H. Jiang, L. P. Lehman, T. Kirkpatrick, E. J. Cotts, and B. Nandagopal, "Influence of Sn Grain Size and Orientation on the Thermomechanical Response and Reliability of Pb-free Solder Joints," *IEEE Transactions on Components and Packaging Technologies*, vol. 31, no. 2, pp. 370–381, 2008, doi: https://doi.org/10.1109/tcapt.2008.916835.

[39] B. Zhou, Q. Zhou, T. R. Bieler, and T. Lee, "Slip, Crystal Orientation, and Damage Evolution During Thermal Cycling in High-Strain Wafer-Level Chip-Scale Packages," *Journal of Electronic Materials*, vol. 44, no. 3, pp. 895–908, 2015, doi: https://doi.org/10.1007/s11664-014-3572-9.

[40] T. R. Bieler *et al.*, "The Role of Elastic and Plastic Anisotropy of Sn in Recrystallization and Damage Evolution During Thermal Cycling in SAC305 Solder Joints," *Journal of Electronic Materials*, vol. 41, no. 2, pp. 283–301, 2012, doi: https://doi.org/10.1007/s11664-011-1811-x.

[41] A. A. Daszki and C. M. Gourlay, "On the 3-D Shape of Interlaced Regions in Sn-3Ag-0.5Cu Solder Balls," *Journal of Electronic Materials*, vol. 50, no. 3, pp. 808–817, 2020, doi: https://doi.org/10.1007/s11664-020-08508-w.

[42] Z. Guo *et al.*, "Slip System-Resolved GNDs and SEDs: A Multi-scale Framework for Predicting Crack Nucleation in Single-Crystal Metals," *Acta Materialia*, vol. 288, pp. 120853–120853, 2025, doi: https://doi.org/10.1016/j.actamat.2025.120853.

[43] J. Pelleg, *Mechanical Properties of Materials*. Dordrecht: Springer Netherlands, 2013. doi: https://doi.org/10.1007/978-94-007-4342-7.

[44] K. Zhang *et al.*, "Characterization of geometrically necessary dislocation evolution during creep of P91 steel using electron backscatter diffraction," *Materials Characterization*, vol. 195, pp. 112501–112501, 2022, doi: https://doi.org/10.1016/j.matchar.2022.112501.

[45] A. J. Schwartz, M. Kumar, and B. L. Adams, Eds., *Electron Backscatter Diffraction in Materials Science*. Boston, MA: Springer US, 2000. doi: https://doi.org/10.1007/978-1-4757-3205-4.

[46] Y. Ateba Betanda, A.-L. Helbert, F. Brisset, M.-H. Mathon, T. Waeckerlé, and T. Baudin, "Measurement of stored energy in Fe–48%Ni alloys strongly cold-rolled using three approaches: Neutron diffraction, Dillamore and KAM approaches," *Materials Science and Engineering: A*, vol. 614, pp. 193–198, 2014, doi: https://doi.org/10.1016/j.msea.2014.07.037.

[47] Jun Yanagimoto, "Deformation (Dislocations)," in *CIRP Encyclopedia of Production Engineering*, Springer Nature, 2016, pp. 1–7. doi: https://doi.org/10.1007/978-3-642-35950-7_6503-3.

[48] A. Singh, S. K. Sharma, and A. Batish, "Dynamic recrystallization during solid state friction stir welding/processing/additive manufacturing: Mechanisms, microstructure evolution, characterization, modeling techniques and challenges," *Critical reviews in solid state and materials sciences*, vol. 50, no. 1, pp. 77–135, 2024, doi: https://doi.org/10.1080/10408436.2024.2391333.

[49] B. Arfaei and E. Cotts, "Correlations Between the Microstructure and Fatigue Life of Near-Eutectic Sn-Ag-Cu Pb-Free Solders," *Journal of Electronic Materials*, vol. 38, no. 12, pp. 2617–2627, 2009, doi: https://doi.org/10.1007/s11664-009-0932-y.

[50] F. Yang and J. C. M. Li, "Deformation behavior of tin and some tin alloys," *Journal of Materials Science: Materials in Electronics*, vol. 18, no. 1–3, pp. 191–210, 2006, doi: https://doi.org/10.1007/s10854-006-9016-4.

[51] L. Yin, L. Wentlent, L. Yang, B. Arfaei, A. Oasaimeh, and P. Borgesen, "Recrystallization and Precipitate Coarsening in Pb-Free Solder Joints During Thermomechanical Fatigue," *Journal of Electronic Materials*, vol. 41, no. 2, pp. 241–252, 2011, doi: https://doi.org/10.1007/s11664-011-1762-2.

[52] T. Gu, Y. Xu, C. M. Gourlay, and T. B. Britton, "In-situ electron backscatter diffraction of thermal cycling in a single grain Cu/Sn-3Ag-0.5Cu/Cu solder joint," *Scripta Materialia*, vol. 175, pp. 55–60, 2019, doi: https://doi.org/10.1016/j.scriptamat.2019.09.003.

[53] X. Jing, K. Luo, K.-W. Paik, P. He, and S. Zhang, "Crack mechanism correlated with Sn grain orientations on Ni metal surface subjected to 1000 thermal shocks," *Journal of Materials Research and Technology*, vol. 26, pp. 1663–1668, 2023, doi: https://doi.org/10.1016/j.jmrt.2023.08.022.

[54] H. Zhong *et al.*, "Resolving localized geometrically necessary dislocation densities in Al-Mg polycrystal via in situ EBSD," *Acta Materialia*, vol. 279, pp. 120290–120290, 2024, doi: https://doi.org/10.1016/j.actamat.2024.120290.

[55] E. B. Romdhane, P. Roumanille, A. Guédon-Gracia, S. Pin, P. Nguyen, and H. Frémont, "From early microstructural evolution to intergranular crack propagation in SAC solders under thermomechanical fatigue," *Microelectronics Reliability*, vol. 126, pp. 114288–114288, 2021, doi: https://doi.org/10.1016/j.microrel.2021.114288.

[56] H. Chen, J. Han, J. Li, and M. Li, "Inhomogeneous deformation and microstructure evolution of Sn–Ag-based solder interconnects during thermal cycling and shear testing," *Microelectronics Reliability*, vol. 52, no. 6, pp. 1112–1120, 2012, doi: https://doi.org/10.1016/j.microrel.2012.01.009.

[57] H. Chen, J. Han, and M. Li, "Localized Recrystallization Induced by Subgrain Rotation in Sn-3.0Ag-0.5Cu Ball Grid Array Solder Interconnects During Thermal Cycling," *Journal of Electronic Materials*, vol. 40, no. 12, pp. 2470–2479, 2011, doi: https://doi.org/10.1007/s11664-011-1782-y.

[58] B. Zhou, T. R. Bieler, T.-K. Lee, and W. Liu, "Characterization of Recrystallization and Microstructure Evolution in Lead-Free Solder Joints Using EBSD and 3D-XRD," *Journal of Electronic Materials*, vol. 42, no. 2, pp. 319–331, 2012, doi: https://doi.org/10.1007/s11664-012-2307-z.

[59] J. B. Libot, J. Alexis, O. Dalverny, L. Arnaud, P. Milesi, and F. Dulondel, "Microstructural evolutions of Sn-3.0Ag-0.5Cu solder joints during thermal cycling," *Microelectronics Reliability*, vol. 83, pp. 64–76, 2018, doi: https://doi.org/10.1016/j.microrel.2018.02.009.

[60] H. Chen, L. Wang, J. Han, M. Li, and H. Liu, "Microstructure, orientation and damage evolution in SnPb, SnAgCu, and mixed solder interconnects under thermomechanical stress," *Microelectronic Engineering*, vol. 96, pp. 82–91, 2012, doi: https://doi.org/10.1016/j.mee.2012.03.005.

[61] S. K. Kang *et al.*, "The Microstructure, Thermal Fatigue, and Failure Analysis of Near-Ternary Eutectic Sn-Ag-Cu Solder Joints," *Materials Transactions*, vol. 45, no. 3, pp. 695–702, Jan. 2004, doi: https://doi.org/10.2320/matertrans.45.695.

[62] H. Chen *et al.*, "Localized recrystallization and cracking of lead-free solder interconnections under thermal cycling," *Journal of materials research*, vol. 26, no. 16, pp. 2103–2116, 2011, doi: https://doi.org/10.1557/jmr.2011.197.

[63] J. Zhao, Y. Mutoh, Y. Miyashita, and S. L. Mannan, "Fatigue crack-growth behavior of Sn-Ag-Cu and Sn-Ag-Cu-Bi lead-free solders," *Journal of Electronic Materials*, vol. 31, no. 8, pp. 879–886, 2002, doi: https://doi.org/10.1007/s11664-002-0199-z.
[64] R. Pandher and R. Healey, "Reliability of Pb-free solder alloys in demanding BGA and CSP applications," in *2008 58th Electronic Components and Technology Conference*, 2008, pp. 2018–2023. doi: https://doi.org/10.1109/ectc.2008.4550261.
[65] A. Lovberg and P.-E. Tegehall, "Transgranular Crack Propagation in Thermal Cycling of SnAgCu Solder Joints," *2019 20th International Conference on Thermal, Mechanical and Multi-Physics Simulation and Experiments in Microelectronics and Microsystems (EuroSimE)*, pp. 1–5, 2019, doi: https://doi.org/10.1109/eurosime.2019.8724507.
[66] A. Ul-Hamid, *A Beginners' Guide to Scanning Electron Microscopy*. Springer International Publishing, 2018. doi: https://doi.org/10.1007/978-3-319-98482-7.
[67] Y. Rodríguez Herrero, K. Lopez Camas, and A. Ullah, "Characterization of biobased materials," in *Advanced Applications of Biobased Materials*, Elsevier BV, 2023, pp. 111–143. doi: https://doi.org/10.1016/b978-0-323-91677-6.00005-2.
[68] R. A. Schwarzer, D. P. Field, B. L. Adams, M. Kumar, and A. J. Schwartz, *Electron Backscatter Diffraction in Materials Science*, 2nd ed. Boston, MA: Springer US, 2009. doi: https://doi.org/10.1007/978-0-387-88136-2.
[69] S. Doddapaneni *et al.*, "Advancements in EBSD Techniques: A Comprehensive Review on Characterization of Composites and Metals, Sample Preparation, and Operational Parameters," *Journal of Composites Science*, vol. 9, no. 132, 2025, doi: https://doi.org/10.3390/%20jcs9030132.
[70] A. D. Herron, S. P. Coleman, K. Q. Dang, D. E. Spearot, and E. R. Homer, "Simulation of kinematic Kikuchi diffraction patterns from atomistic structures," *MethodsX*, vol. 5, pp. 1187–1203, 2018, doi: https://doi.org/10.1016/j.mex.2018.09.001.
[71] S. Vespucci, "Direct electron imaging of energy filtered EBSD patterns using a CMOS hybrid pixel detector," in *17th International Workshop on Radiation Imaging Detectors (iWoRiD)* , University of Strathclyde, Glasgow, 2015.
[72] M. C. Nebbar, M. Zidani, S. Messaoudi, T. Abid, A. Kisrane-Bouzidi, and T. Baudin, "Wire Drawing Effect on Microstructural and Textural Evolution in Medium Carbon Steel Wires," *Defect and Diffusion Forum*, vol. 406, pp. 505–510, 2021, doi: https://doi.org/10.4028/www.scientific.net/ddf.406.505.
[73] S. Swapp, "Electron Backscatter Diffraction (EBSD)," *Science Education Resource Center at Carleton College*, 2024. https://serc.carleton.edu/msu_nanotech/methods/ebsd.html
[74] T. B. Britton *et al.*, "Tutorial: Crystal orientations and EBSD — Or which way is up?," *Materials Characterization*, vol. 117, pp. 113–126, 2016, doi: https://doi.org/10.1016/j.matchar.2016.04.008.
[75] H. Mubarak, "Dégradation de l'acier inoxydable soumis à la contrainte : L'influence des contraintes sur la cinétique de passivation, et la cristallographie de la fissuration dans des milieux acides," PhD Dissertation, École Nationale Supérieure des Arts et Métiers, 2016.
[76] A. J. Wilkinson and T. Ben. Britton, "Strains, planes, and EBSD in materials science," *Materials Today*, vol. 15, no. 9, pp. 366–376, Sep. 2012, doi: https://doi.org/10.1016/s1369-7021(12)70163-3.
[77] S. Tsukimoto *et al.*, "Correlation between Local Strain Distribution and Microstructure of Grinding-Induced Damage Layers in 4H-SiC(0001)," *Materials science forum*, vol. 897, pp. 177–180, 2017, doi: https://doi.org/10.4028/www.scientific.net/msf.897.177.
[78] J. Wu and E. Choo, "Mining EDS-EBSD Data to Study Microstructure of Solder Bump with Completely Unknown Intermetallics," in *2022 IEEE 39th International Electronics Manufacturing Technology Conference (IEMT)*, 2022, pp. 1–4. doi: https://doi.org/10.1109/iemt55343.2022.9969507.
[79] Y. Zhang, Y. Yan, S. Vollebregt, and G. Zhang, "In Situ Analysis of Copper Microstructures in Electromigration Using SEM-EBSD Techniques," in *2024 IEEE 74th Electronic Components and Technology Conference (ECTC)*, 2024, pp. 1317–1321. doi: https://doi.org/10.1109/ectc51529.2024.00214.

[80] M. N. Gussev, D. A. McClintock, T. S. Byun, and T. G. Lach, "Recent progress in analysis of strain-induced phenomena in irradiated metallic materials and advanced alloys using SEM-EBSD in-situ tensile testing," *Current Opinion in Solid State and Materials Science*, vol. 28, pp. 101132–101132, 2023, doi: https://doi.org/10.1016/j.cossms.2023.101132.

[81] C. Cui *et al.*, "Correlative, ML-based and non-destructive 3D-analysis of intergranular fatigue cracking in SAC305-Bi solder balls," *npj Materials Degradation*, vol. 8, no. 1, 2024, doi: https://doi.org/10.1038/s41529-024-00456-8.

[82] T. Krämer, L. Eisenhut, L. Germain, D. Rupp, E. Detemple, and C. Motz, "Assessment of EBSD Analysis and Reconstruction Methods as a Tool for the Determination of Recrystallized Fractions in Hot-Deformed Austenitic Microstructures," *Metallurgical and Materials Transactions A*, vol. 49, no. 7, pp. 2795–2802, 2018, doi: https://doi.org/10.1007/s11661-018-4593-4.

[83] A. Ayad, M. Ramoul, A. D. Rollett, and F. Wagner, "Quantifying primary recrystallization from EBSD maps of partially recrystallized states of an IF steel," *Materials Characterization*, vol. 171, pp. 110773–110773, 2020, doi: https://doi.org/10.1016/j.matchar.2020.110773.

[84] T. Baudin, H. Azzeddine, F. Brisset, Y. Huang, and T. G. Langdon, "Estimating dislocation density from electron backscatter diffraction data for an AZ31/Mg-0.6Gd hybrid alloy fabricated by high-pressure torsion," *The Philosophical Magazine A Journal of Theoretical Experimental and Applied Physics*, vol. 104, no. 6–8, pp. 389–405, 2024, doi: https://doi.org/10.1080/14786435.2024.2308203.

[85] Y. Xu, J. Xian, R. J. Coyle, C. M. Gourlay, and F. P. E. Dunne, "Mechanistic understanding of microstructural effects on the thermal fatigue resistance of solder joints," *Journal of the Mechanics and Physics of Solids*, vol. 187, pp. 105623–105623, 2024, doi: https://doi.org/10.1016/j.jmps.2024.105623.

[86] Y. Wu, J. Uusitalo, and A. J. DeArdo, "Stored Energy Evaluation for High Strength Dual-Phase Steels with Different Pre-annealing Conditions," *Metallurgical and Materials Transactions A*, vol. 51, no. 9, pp. 4727–4741, 2020, doi: https://doi.org/10.1007/s11661-020-05890-2.

[87] M. R. Marks, K. Y. Cheong, and Z. Hassan, "A review of laser ablation and dicing of Si wafers," *Precision Engineering*, vol. 73, pp. 377–408, 2022, doi: https://doi.org/10.1016/j.precisioneng.2021.10.001.

[88] NXP Semiconductors, "CLC - Laser (UV) Investigation - Company Internal," 2020.

[89] X. Meng and J. Zhao, "An evaluation of Ar ion milling in TEM sample preparation by energy-filtered TEM technique," *Vacuum*, vol. 222, pp. 112980–112980, 2024, doi: https://doi.org/10.1016/j.vacuum.2024.112980.

[90] H. Ito and Y. Inagi, "Hitachi's State-of-the-Art Ion Milling Systems," THE HITACHI SCIENTIFIC INSTRUMENT NEWS: Technical magazine of Electron Microscope and Analytical Instruments, vol. 10, pp. 22 – 29, 2018.

[91] L. Dieterle, B. Butz, and E. Müller, "Optimized Ar+-ion milling procedure for TEM cross-section sample preparation," *Ultramicroscopy*, vol. 111, no. 11, pp. 1636–1644, 2011, doi: https://doi.org/10.1016/j.ultramic.2011.08.014.

[92] T. Dunlop, O. Kesteven, F. De Rossi, P. Davies, T. Watson, and C. Charbonneau, "Exploring the Infiltration Features of Perovskite within Mesoporous Carbon Stack Solar Cells Using Broad Beam Ion Milling," *Materials*, vol. 14, no. 19, p. 5852, 2021, doi: https://doi.org/10.3390/ma14195852.

[93] E. Harper and J. J. Cuomo, "Material Processing with Broad-Beam Ion Sources," *Annual Review of Materials Science*, vol. 13, no. 1, pp. 413–439, 1983, doi: https://doi.org/10.1146/annurev.ms.13.080183.002213.

[94] A. U. Telang, T. R. Bieler, A. Zamiri, and F. Pourboghrat, "Incremental recrystallization/grain growth driven by elastic strain energy release in a thermomechanically fatigued lead-free solder joint," *Acta Materialia*, vol. 55, no. 7, pp. 2265–2277, 2007, doi: https://doi.org/10.1016/j.actamat.2006.11.023.

[95] R. D. Doherty *et al.*, "Current issues in recrystallization: a review," *Materials Science and Engineering: A*, vol. 238, no. 2, pp. 219–274, 1997, doi: https://doi.org/10.1016/s0921-5093(97)00424-3.

[96] B. Arfaei *et al.*, "The effect of Sn grain number and orientation on the shear fatigue life of SnAgCu solder joints," in *2008 Electronic Components and Technology Conference*, 2008, pp. 459–465. doi: https://doi.org/10.1109/ectc.2008.4550012.

[97] P. Børgesen *et al.*, "A Mechanistic Thermal Fatigue Model for SnAgCu Solder Joints," *Journal of Electronic Materials*, vol. 47, no. 5, pp. 2526–2544, 2018, doi: https://doi.org/10.1007/s11664-018-6121-0.

APPENDIX

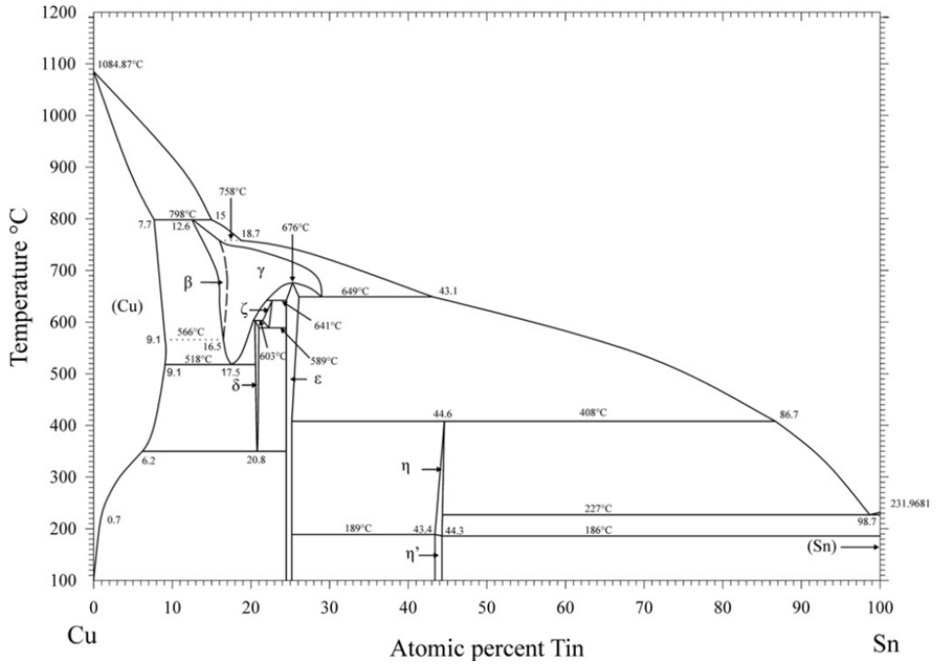

Figure A1: Sn-Cu binary phase diagram. In SAC solders, $Cu_6Sn_5(\eta)$ and $Cu_3Sn(\varepsilon)$ are observed to form, corresponding to a primitive hexagonal and a base-centered orthorhombic structure, respectively. *[30]*

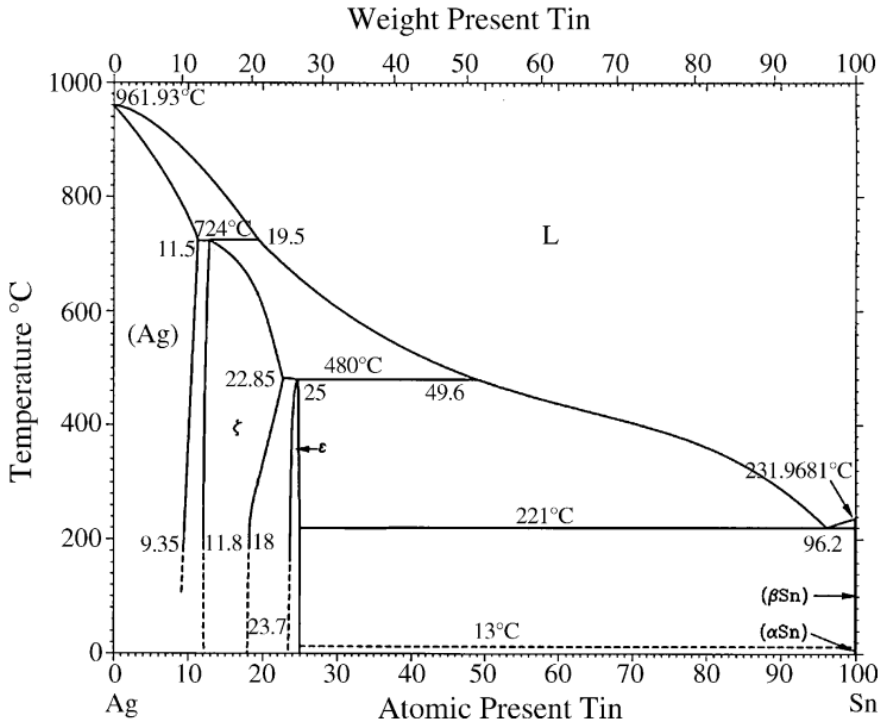

Figure A2: The Sn-Ag binary phase diagram. In SAC solders, $Ag_3Sn(\varepsilon)$ is observed to form, corresponding to an orthorhombic short-range ordered structure *[27]*

Table A1: Lattice parameters of β-Sn and IMCs [8]

Phase	Structure	a (Å)	b (Å)	c (Å)
β-Sn	body-centered tetragonal	5.83	5.83	3.18
Ag_3Sn	orthorhombic	5.97	4.78	5.18
Cu_3Sn	orthorhombic	5.53	47.75	4.32
Cu_6Sn_5	hexagonal	4.19	4.19	5.086

Pure β-Sn stiffness matrix [26],

$$[C]_{\beta-Sn} = \begin{bmatrix} 72.3 & 59.4 & 35.8 & 0 & 0 & 0 \\ 59.4 & 72.3 & 35.8 & 0 & 0 & 0 \\ 35.8 & 35.8 & 88.4 & 0 & 0 & 0 \\ 0 & 0 & 0 & 22 & 0 & 0 \\ 0 & 0 & 0 & 0 & 22 & 0 \\ 0 & 0 & 0 & 0 & 0 & 24 \end{bmatrix} \text{ Gpa} \qquad \text{(A1)}$$

where, $C_{11} = C_{22} = 72.3$ GPa, is the stiffness along the [100] and [010] direction respectively, and $C_{33} = 88.4$ GPa, the stiffness along [001] direction.

Table A2: Slip systems observed in β-Sn, where CRSS ratio, is the Critical Resolved Shear Stress ratio, m, the Schmid factor and m_w, the weighted Schmid factor [52]

Family	**Slip system**		**CRSS ratio**	**m**	**m_w**
1	1	$(100)[001]$	1	0.238	0.238
	2	$(010)[001]$	1	0.012	0.012
2	3	$(110)[001]$	1	0.177	0.177
	4	$(1\bar{1}0)[001]$	1	0.160	0.160
3	5	$(100)[010]$	1.05	0.048	0.046
	6	$(010)[100]$	1.05	0.048	0.046
4	7	$(110)[1\bar{1}1]/2$	1.1	0.500	0.454
	8	$(110)[\bar{1}11]/2$	1.1	0.372	0.344
	9	$(1\bar{1}0)[111]/2$	1.1	0.494	0.449
	10	$(1\bar{1}0)[\bar{1}\bar{1}1]/2$	1.1	0.378	0.344
5	11	$(110)[1\bar{1}0]$	1.2	0.467	0.389
	12	$(1\bar{1}0)[110]$	1.2	0.467	0.389
6	13	$(010)[101]$	1.25	0.048	0.038
	14	$(010)[10\bar{1}]$	1.25	0.036	0.029
	15	$(100)[011]$	1.25	0.156	0.125
	16	$(100)[01\bar{1}]$	1.25	0.072	0.058
7	17	$(001)[100]$	1.3	0.238	0.183
	18	$(001)[010]$	1.3	0.012	0.009
8	19	$(001)[110]$	1.4	0.177	0.126
	20	$(001)[1\bar{1}0]$	1.4	0.160	0.114
9	21	$(101)[10\bar{1}]$	1.5	0.497	0.332
	22	$(10\bar{1})[101]$	1.5	0.240	0.160
	23	$(011)[01\bar{1}]$	1.5	0.018	0.012
	24	$(01\bar{1})[011]$	1.5	0.031	0.021
10	25	$(121)[\bar{1}01]$	1.5	0.384	0.256
	26	$(1\bar{2}1)[\bar{1}01]$	1.5	0.334	0.223
	27	$(\bar{1}21)[101]$	1.5	0.140	0.093
	28	$(\bar{1}\bar{2}1)[101]$	1.5	0.207	0.138
	29	$(211)[0\bar{1}1]$	1.5	0.063	0.042
	30	$(\bar{2}11)[0\bar{1}1]$	1.5	0.037	0.025
	31	$(\bar{2}\bar{1}1)[011]$	1.5	0.086	0.057
	32	$(2\bar{1}1)[011]$	1.5	0.131	0.087

Table A3: Slip system families used for slip activity analysis

SS Family	Slip system
SS1	{100}<001>
SS2	{110}<001>
SS3	{100}<010>
SS4	{110}<1$\bar{1}$1>
SS5	{110}<1$\bar{1}$0>
SS6	{010}<10$\bar{1}$>
SS7	{001}<100>
SS8	{001}<110>
SS9	{101}<10$\bar{1}$>
SS10	{121}<$\bar{1}$01>

Table A4: Corresponding thermal cycling stage of solder bumps

Bump No.	Stage 0	Stage 1	Stage 2	Stage 3	Stage 4	Stage 5
2		x				
3			x			
5			x			
18				x		
22				x		
16					x	
19					x	
13						x
14						x
34						
35						
4	x	x	x	x	x	x
8	x	x	x	x	x	x

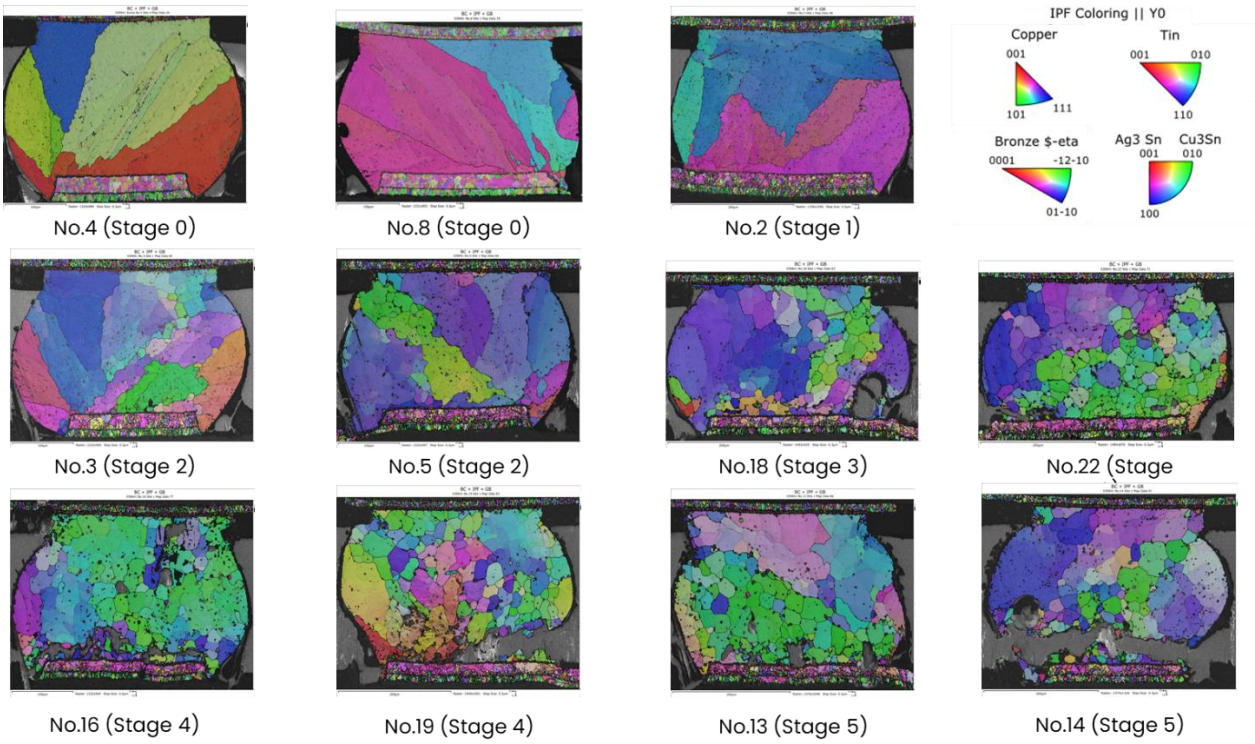

Figure A3: IPF-colored EBSD Maps of cross-sectioned solder bumps showing microstructure and grain orientations relative to the y-axis.

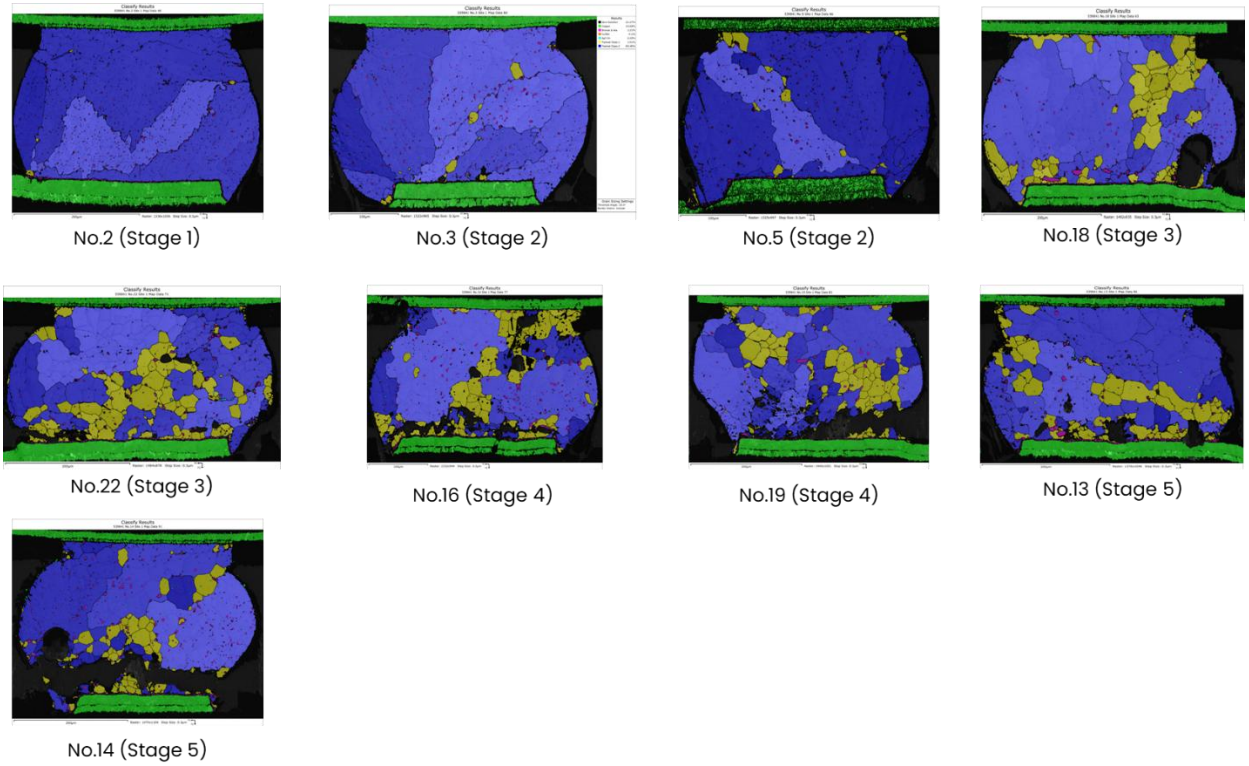

Figure A4: Classification between recrystallized and deformed grains. Yellow grains correspond to recrystallized while blue to deformed grains.

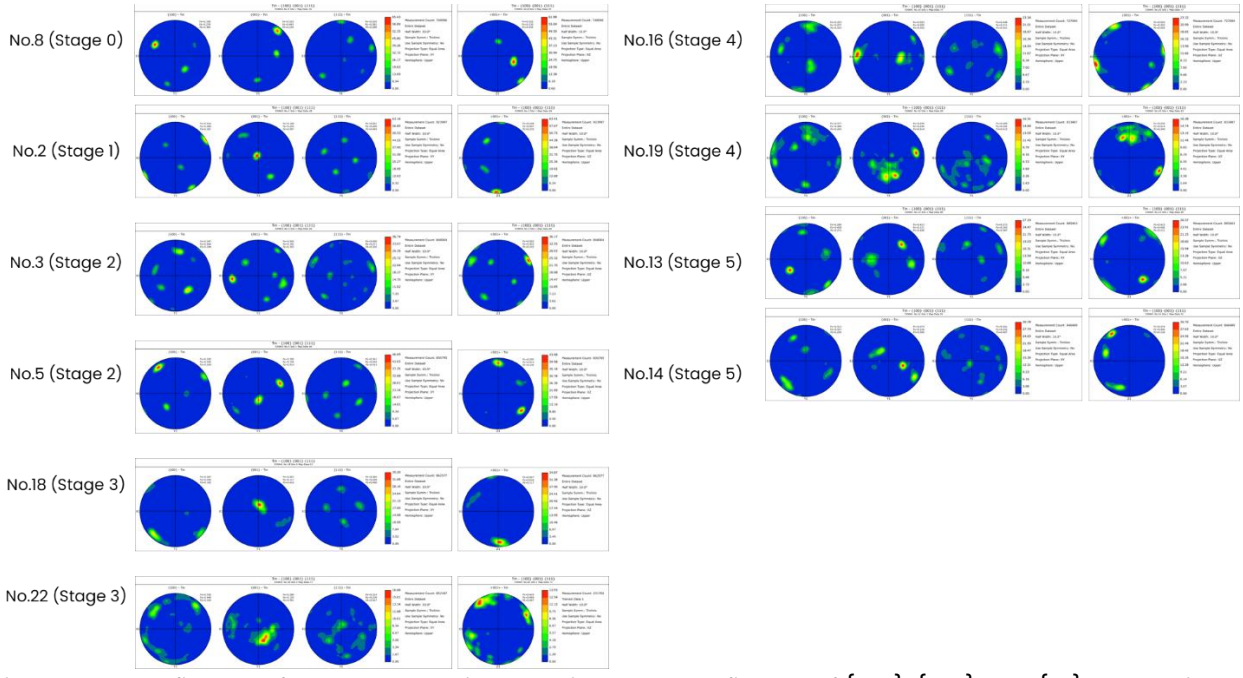

Figure A5: Pole figures of all samples. Triple sets include pole figures of {100}, {001} and {111}, respectively and are projected in the XY plane. Individual pole figures correspond to [001]Sn direction projected in the XZ plane.

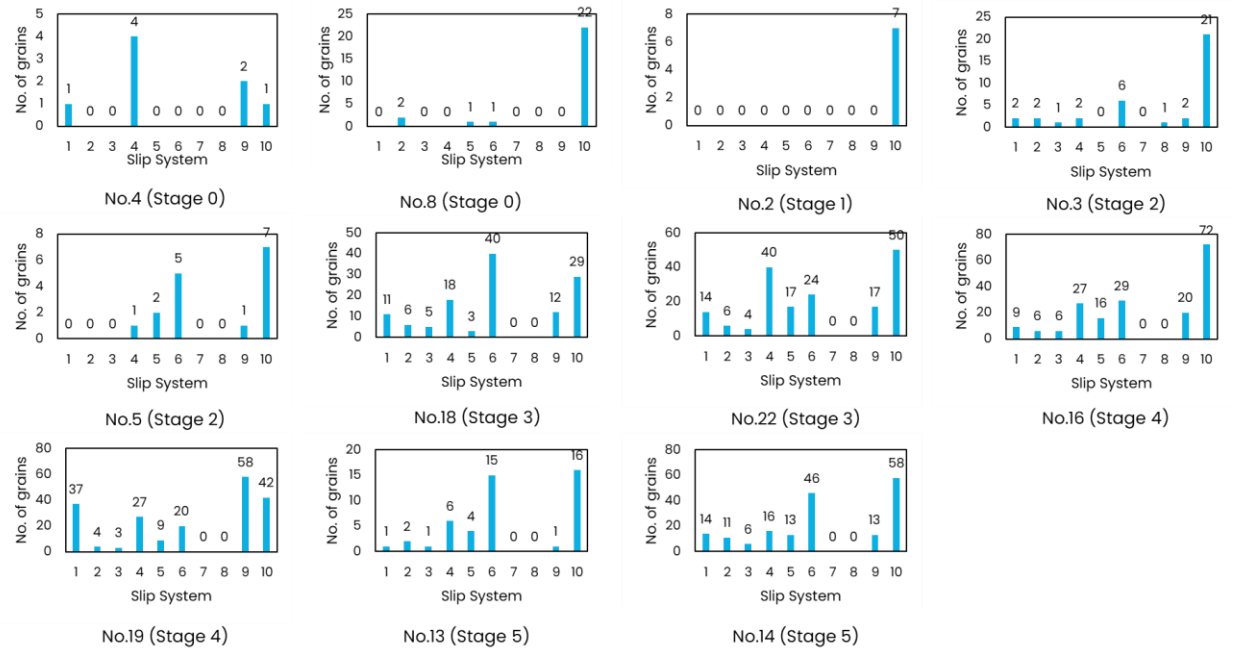

Figure A6: Slip activity in recrystallized grains

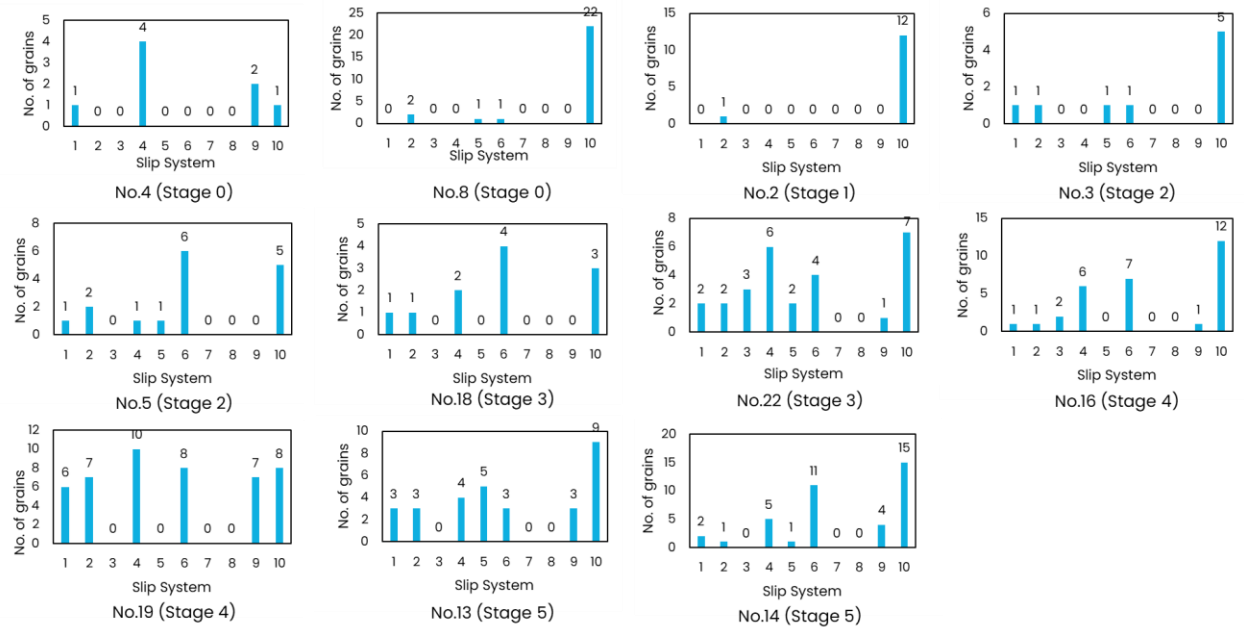

Figure A7: Slip activity in deformed grains

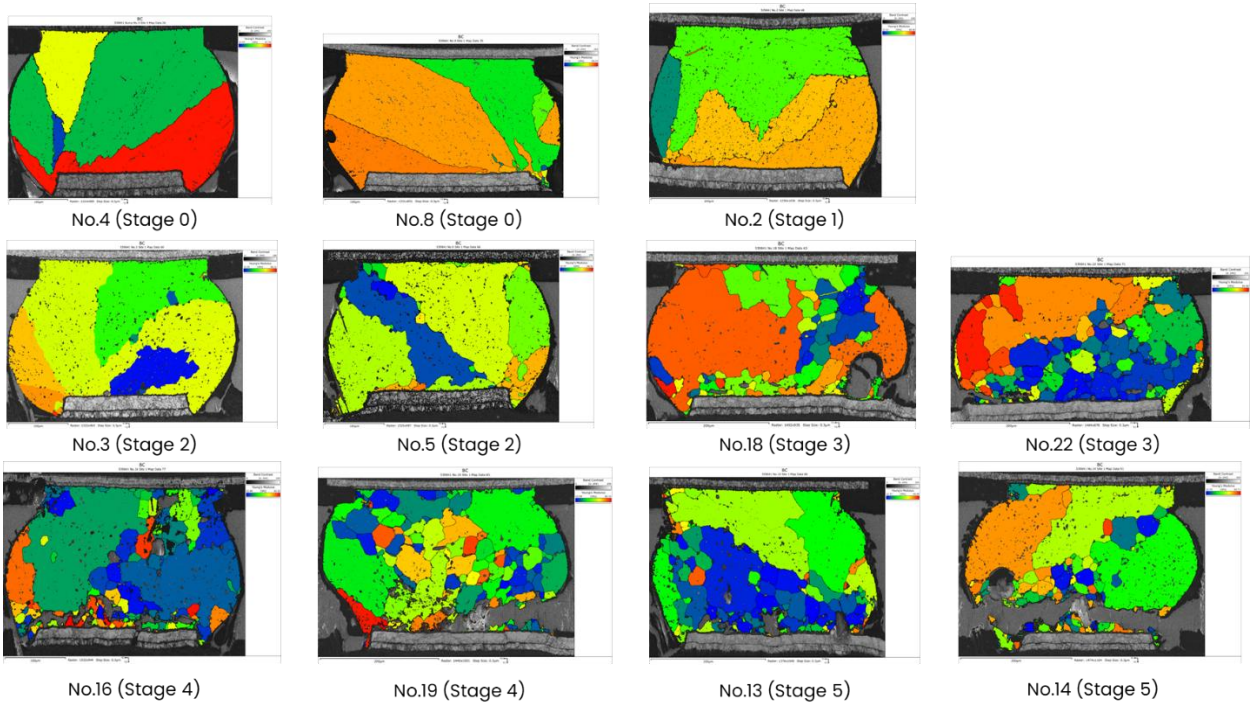

Figure A8: Evolution of Young's Modulus in Sn grains (loading direction along Y-axis)